

Efficient, Equivariant Predictions of Distributed Charge Models

Eric D. Boittier and Markus Meuwly*

Department of Chemistry, University of Basel, Klingelbergstrasse 80, CH-4056 Basel, Switzerland.

E-mail: m.meuwly@unibas.ch

Abstract

A machine learning (ML) based, equivariant neural network for constructing distributed charge models (DCMs) of arbitrary resolution - DCM-net - is presented. DCMs efficiently and accurately model the anisotropy of the molecular electrostatic potential (ESP) and go beyond the point charge representation used in conventional molecular mechanics (MM) energy functions. This is particularly relevant for capturing the conformational dependence of the ESP (internal polarization) and chemically relevant features such as lone pairs or σ -holes. Across conformational space, the learned charge positions from DCM-net are stable and continuous. Across the QM9 chemical space, two-charge-per-atom models achieve accuracies comparable to fitted atomic dipoles for previously unseen molecules (0.75 (kcal/mol)/ e). Three- and four-charge-per-atom models reach accuracies competitive with atomistic multipole expansions up to quadrupole level (0.55 (kcal/mol)/ e). Pronounced improvements of the ESP are found around O- and F-atoms both of which are known to feature strongly anisotropic fields, and for aromatic systems. Across the QM9 reference data set, molecular dipole moments improve by ~ 0.1 D compared with fitted monopoles. Transfer learning on dipeptides yields a 0.2 (kcal/mol)/ e ESP improvement for unseen samples and a two-fold MAE

reduction for molecular dipole versus fitted monopoles. Overall, DCM-net offers a fast and physically meaningful approach to generating distributed charge models for running pure ML- or mixed ML/MM-based molecular simulations.

February 10, 2026

1 Introduction

The electrostatic potential (ESP) around a molecule can be used to explain a wide range of molecular properties related to structure, bonding, stability, and reactivity, among others.^{1–5} The ESP can be highly anisotropic leading to a variety of chemically relevant features including "lone pairs" and " σ -holes", for example, which cannot be modeled with atom-centered charges.^{6–9} By reducing the representation of the local electrostatic environment to atomic multipoles or point charges (PCs), the true anisotropic electrostatic potential of the molecule is neglected.¹⁰ A successful approach to modeling the molecular electrostatic potential has been to use atom-centered multipoles (MTPs) to a given order.^{10–13} Often, this expansion is truncated at the atomic quadrupole moment for all atoms except hydrogens for which a PC representation is usually sufficient.^{10,14–16} Including higher order atomic multipoles has been successful in crystal structure prediction¹⁷ and modeling interaction energies using force fields.^{18–20} These atomic multipole expansions can be obtained from the electron density of the wavefunction, using techniques such as the Minimal Basis Iterative Stockholder (MBIS) procedure.²¹

The quantum theory of atoms in molecules (QTAIM) suggests features in the molecular density, such as bond critical points, which are well described using distributed multipoles.²² Likewise, PC-based energy functions have been supplemented by off-center PCs in the OPLS force field to model the anisotropy of the ESP,^{7,8} sometimes referred to as 'extra charge' or lone pair sites, introduced in the AMBER force field to better describe hydrogen bonding

and halogen interactions,^{23,24} or virtual interaction sites in GROMACS.²⁵ More generally, an atomic multipole expansion can be approximated using multiple point charges arranged around an atomic center, which leads to "distributed charge models" (DCMs).²⁶ Formally, to obtain a DCM-representation of the multipole expansion up to the quadrupole level, six charges per atom are required.²⁶ Like atomic multipoles,¹¹ improvements in interaction energies have also been observed with distributed charge models.²⁷ The derived multipoles are sensitive to the local atomic environment and therefore exhibit pronounced conformational dependence^{11,28} suggesting that a static representation of atomic multipoles may not be sufficient in some cases. Geometry-dependent distributed charge models to capture effects of bond polarization have also been considered.^{29,30} When modeling the molecular ESP, significant redundancy in electrostatic parameters has been observed.³¹ This has justified the use of minimal distributed charges³² which involved fitting charges to atomic environments and combining these initial guesses using differential evolution (DE) to obtain a model with low complexity and sufficient quality.³²

In force-field development, it is often desirable to obtain 'transferable' parameters across some predefined chemical space whereby topologically similar atoms are assigned the same 'atom type' to reduce the complexity of the model.^{16,23,27,33} Ideally, these shared parameters should be accurate for molecules not explicitly included during parametrization.^{13,34} Transferable multipoles were investigated by Bereau and coworkers^{13,34} using predefined reference frames based on handcrafted atom types^{11,13} Alternatively, transferability can be obtained without predefined reference frames by using a molecular frame of reference, which can be derived from the principal moments of inertia.^{35,36} Neural networks with directional features can learn a 'representation' of local reference frames from the data which may improve transferability.³⁷ The difference between 'hand-crafted' versus learnt local reference frames is analogous to manually constructed features used in Behler–Parrinello atomistic neural networks versus data-driven features learnt by message-passing networks such as PhysNet.³⁸

Geometric deep learning^{39,40} has emerged as a promising strategy for problems where strong inductive priors stemming from the laws of physics, such as the invariance of energy with respect to rotations and translations, can be leveraged to create efficient, performant, and physically meaningful models.^{39,40} Equivariant neural networks are data-efficient, universal approximators for tasks where inherent symmetries exist, such as rotational equivariance.^{41–43} For example, vector quantities such as dipole moments should rotate with the molecule.^{35,36} Equivariant neural networks have been applied to the prediction of atomic multipole expansions.³⁷ By including higher order many-body messages based on spherical harmonics, techniques such as Multiple Atomic Cluster Expansion (MACE),⁴⁴ as well as equivariant attention mechanisms,⁴⁵ have shown state-of-the-art accuracy in a variety of tasks, such as predicting molecular dipole moments. This approach has also been generalized to Cartesian tensors, which may require fewer parameters.⁴⁶

Kernel-based methods using rotationally equivariant features have also been used to model the molecular dipole moment.⁴⁷ If only scalar properties are of interest, traditional deep neural networks are sufficient, e.g., for predicting electrostatic parameters for the polarizable Drude classical force field.⁴⁸ Although strictly equivariant models have garnered significant attention, alternatives which weaken these requirements have been found to provide better performance when large amounts of training data and compute resources are available.^{49,50} For instance, the Point Edge Transformer,⁴⁹ a graph neural network where each message-passing layer is given by an arbitrarily deep transformer. Furthermore, strategies such as data augmentation⁵¹ have been employed whereby the input and output features are rotated arbitrarily during training.⁵¹ Learning a representation of the density has been explored via construction of the Hamiltonian matrix in a block-wise manner from equivariant representations,⁵² as well as grid based electron density learning schemes.^{53,54}

The present work describes “DCM-net” (distributed charge model network) which is an equivariant neural network for the prediction of distributed charges - trained to minimize the error of the molecular ESP. The model predicts up to n_{DC} distributed charges per atom. The performance of the model at reproducing the ESP and molecular dipole moment is assessed on a hold-out set of unseen structures to assess the model’s transferability.

2 Methods

First, a cursory background on molecular electrostatics is presented, then the SO(3)-equivariant architecture is described, along with data curation, training objectives, and various evaluations.

2.1 Electrostatics, Multipoles, and Distributed Charges

The electrostatic potential (ESP) at a point \mathbf{r} arising from a continuous charge distribution $\rho(\mathbf{r}')$, omitting the prefactor $(4\pi\epsilon_0)^{-1}$ for clarity, is

$$\text{ESP}(\mathbf{r}) \sim \int_{V'} \frac{\rho(\mathbf{r}')}{|\mathbf{r} - \mathbf{r}'|} dV' \quad (1)$$

Expanding the ESP in a Taylor series about a chosen center, typically the center of charge or an atomic nucleus, yields the familiar multipole expansion.⁵⁵ In spherical coordinates, and truncated at maximum angular momentum ℓ_{\max} , the ESP at coordinates (r, θ, ϕ) can be approximated by

$$\text{ESP}(r, \theta, \phi) \approx \sum_{\ell=0}^{\ell_{\max}} \sum_{m=-\ell}^{\ell} Q_{\ell}^m Y_{\ell}^m(\theta, \phi) R_{\ell}(r) \quad (2)$$

Here, $Y_{\ell}^m(\theta, \phi)$ are spherical harmonics, $R_{\ell}(r)$ are radial functions determined by the order of the multipole, and the coefficients Q_{ℓ}^m , the multipole moments, encode the angular components of the charge distribution.^{2,55,56} These coefficients can be derived from $\rho(\mathbf{r}')$, though they depend on the choice of partitioning scheme when applied to atoms in molecules, and

are therefore not unique.^{2,28} The lowest-order terms correspond to familiar physical quantities (see Figure 1a; $\ell = 0$: monopole (total charge), $\ell = 1$: dipole, $\ell = 2$: quadrupole).

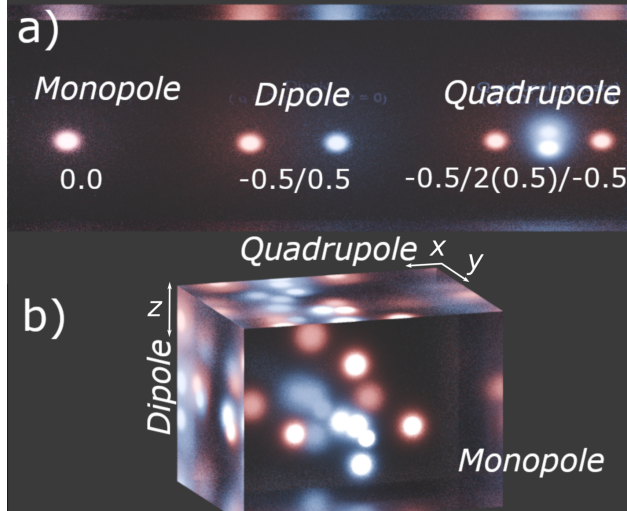


Figure 1: Reproducing the ESP: a graphical illustration of equations 3, 4, and 5 using a computer render of colored ‘point lights’ in glass. a) The standard point charge representations of the monopole, dipole, and quadrupole moments. b) Aligning the dipole perpendicularly to the quadrupole directions gives a distributed charge solution for a system with vanishing monopole moment. Distributed charges offer a parameter efficient approach to fitting the ESP in volumes of interest (outside the glass, i.e. van der Waals region).

A finite set of symmetrically arranged monopoles can exactly reproduce the low-order multipoles; for example, a system of six judiciously placed charges would be correct up to quadrupole order, defining the monopole (placed at the center of mass), dipole (two charges placed at some coordinates scaled by r), and selected quadrupole components (placed at some coordinate scaled by r^2).^{26,32} In this fashion, the number of charges would scale as $O((1 + \ell)^2 - l + 1)$. For example, the total charge (referred to here as the ‘monopole’) is

$$Q_0^0 = q = \sum_{i=1}^6 q_i \quad (3)$$

The dipole moments in the z , x , and y directions (expressed using real spherical harmonic

convention for Q_1^m) are

$$Q_1^0 = \mu_z = \sum_{i=1}^6 q_i r_{z,i}, \quad Q_1^{-1} = \mu_x = \sum_{i=1}^6 q_i r_{x,i}, \quad Q_1^1 = \mu_y = \sum_{i=1}^6 q_i r_{y,i} \quad (4)$$

and the (non-redundant) quadrupole terms are

$$Q_2^0 = \Theta_{zz} = \sum_{i=1}^6 \frac{1}{2} q_i (3r_{z,i}^2 - r_i^2), \quad Q_2^{2c} = \frac{1}{\sqrt{3}} (\Theta_{xx} - \Theta_{yy}) = \sum_{i=1}^6 \frac{3}{4} q_i (r_{x,i}^2 - r_{y,i}^2) \quad (5)$$

Here, $r_{x,i}, r_{y,i}, r_{z,i}$ are the Cartesian coordinates of each point charge q_i in a local coordinate frame (typically the principal axis system), and $r_i^2 = r_{x,i}^2 + r_{y,i}^2 + r_{z,i}^2$. This construction is illustrated in Figure 1 using a computer render of colored ‘point lights’ in glass. The first three moments are reproduced when the dipole moment is aligned along the z -direction, orthogonal to the quadrupole moment in the x - and y -directions. While this example uses six charges to exactly reproduce the leading multipole moments, fewer charges can be used to generate approximate representations of the ESP, giving rise to the minimal distributed charge model (MDCM).³² The use of distributed point charges in this way underlies the DCM formalism employed in the present work.

This motivates a compact representation of anisotropy via a small set of off-center charges; DCM-net learns their positions and magnitudes from local environments while preserving rotational behavior.^{7,8,24}

2.2 SO(3)-Equivariant Graph Neural Network

DCM-net predicts the charge and position of a set of distributed monopoles to represent the molecular electrostatic potential (ESP). It is implemented in JAX⁵⁷ using the e3x package.⁵⁸ The model employs a message-passing architecture composed of equivariant dense layers and

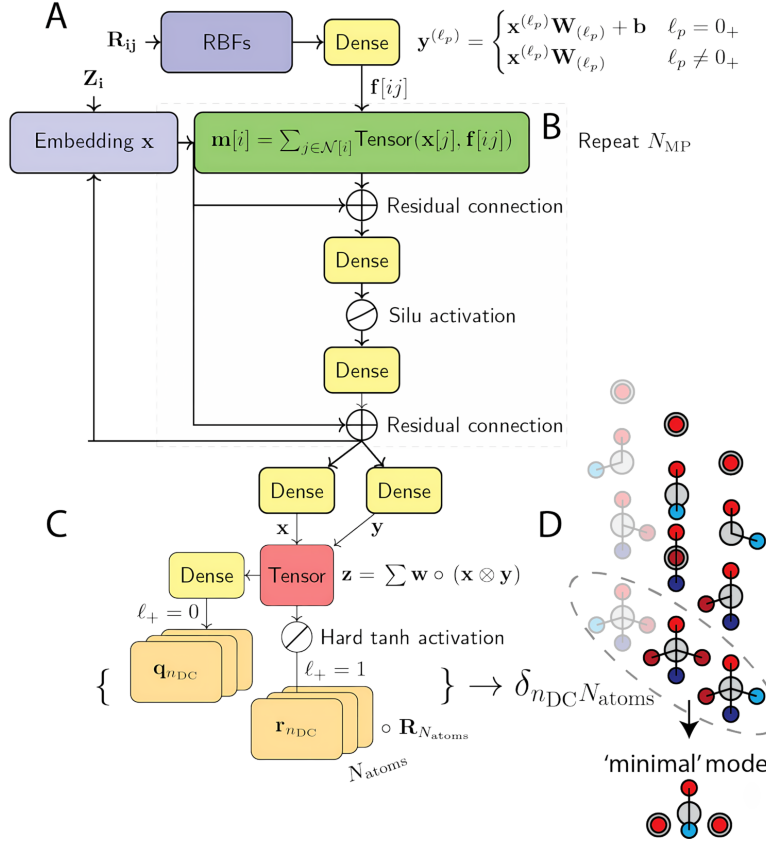


Figure 2: The architecture of DCM-net model. (A) The inputs to the network are atomic numbers and positions expanded into atom-atom distances. (B) During the message passing phase, the hidden representation is updated over N_{MP} iterations using the message passing operation (green). Dense layers (Eq. 6) and tensor products (Eq. 7) are shown in yellow and red, respectively. (C) The final output is split between scalar features (monopoles) and vector-like features (charge displacements relative to atomic centers). (D) Predictions using n_{DC} distributed charges (red, blue) per atom (gray) can be combined and optimized to create ‘minimal’ models with acceptable accuracy and improved computational efficiency, and can be used in molecular dynamics simulations.

tensor product operations, described below and illustrated in Figure 2. The choice of an equivariant architecture is motivated, in the SI (Figures 7 and 8), by way of a toy example.

An equivariant dense layer operates analogously to a standard multilayer perceptron when propagating scalar (rotation-invariant) features, with weights \mathbf{W} and biases \mathbf{b} . For tensor-valued features (e.g. the dipole moment vector \mathbf{D}), the bias term is omitted to preserve $SO(3)$ equivariance (see ‘Dense layer’ in Figure 2A).^{41,42} Let ℓ denote the degree of the spherical

harmonic (or equivalently, the rank of the irreducible representation), and let $p = (-1)^\ell$ denote the parity under inversion. The layer transformation is:

$$\mathbf{y}^{(\ell)} = \begin{cases} \mathbf{x}^{(\ell)} \mathbf{W}^{(\ell)} + \mathbf{b}, & \ell = 0 \text{ (scalar)} \\ \mathbf{x}^{(\ell)} \mathbf{W}^{(\ell)}, & \ell > 0 \text{ (tensor)} \end{cases} \quad (6)$$

Tensor features are combined via tensor product operations (denoted “Tensor” in Figure 2B and C), which mix compatible input irreducible representations based on angular momentum coupling rules (see below).³⁵ The tensor product uses learnable weights $\mathbf{w}_{(l_1, l_2, l_3)}$, and computes the coupled output features $\mathbf{z}^{(l_3)}$:

$$\mathbf{z}^{(l_3)} = \sum_{(l_1, l_2) \in V} \mathbf{w}_{(l_1, l_2, l_3)} \circ (\mathbf{x}^{(l_1)} \otimes^{(l_3)} \mathbf{y}^{(l_2)}) \quad (7)$$

The tensor product $\otimes^{(l_3)}$ couples input features using Clebsch–Gordan coefficients:^{35,36}

$$(\mathbf{x}^{(l_1)} \otimes \mathbf{y}^{(l_2)}) m_3^{(l_3)} = \sum m_1 = -l_1 \sum_{m_2=-l_2}^{l_2} C_{l_1, l_2, l_3}^{m_1, m_2, m_3}, x_{m_1}^{(l_1)} y_{m_2}^{(l_2)} \quad (8)$$

Here, $C_{l_1, l_2, l_3}^{m_1, m_2, m_3}$ are the Clebsch–Gordan coefficients that couple angular momenta l_1 and l_2 to l_3 and similarly for the projections m_1 , m_2 , and m_3 , which amounts to ensure that the coupled feature transforms according to the l_3 irreducible representation of SO(3).

In Eq. 8 the set V contains combinations of (l_1, l_2) such that $C_{l_1, l_2, l_3}^{m_1, m_2, m_3} \neq 0$ given output l_3 . Each $\mathbf{w}_{(l_1, l_2, l_3)} \in \mathbb{R}^{1 \times 1 \times F}$ is a learnable weight shared across features (broadcast over all atoms). The element-wise product \circ denotes broadcasting over tensor dimensions.

Input features $\mathbf{x} \in \mathbb{R}^{P_1 \times (L_1+1)^2 \times F}$ and $\mathbf{y} \in \mathbb{R}^{P_2 \times (L_2+1)^2 \times F}$ are indexed over irreducible representation channels $(L_i + 1)^2$ corresponding to the number of real spherical harmonic components up to and including angular momentum L_i . The parity index $P_i = 2$ if pseudotensors are

included, and $P_i = 1$ otherwise. The output is $\mathbf{z} \in \mathbb{R}^{P_3 \times (L_3+1)^2 \times F}$.

Initial atomic embeddings \mathbf{x} are obtained from atomic numbers \mathbf{Z} via a learnable embedding layer. Interatomic displacement vectors \mathbf{R}_{ij} are computed from atom positions and expanded in a product basis consisting of radial and angular terms:

$$\Phi_{lm}(r, \theta, \phi) = B_n(r)Y_{lm}(\theta, \phi) \quad (9)$$

where Y_{lm} are real spherical harmonics and $B_n(r)$ are radial basis functions. Following previous work,⁵⁸ Bernstein polynomials for $B_n(r)$ are used, due to their compact support and flexibility when modeling exponential decay as a basis with spherical harmonics parametrized by the maximum degree and the number of basis functions. Reciprocal Bernstein radial functions modified by a smooth cutoff function were also included in the features.⁵⁸ The standard message passing scheme involves the application of the graph convolution ϕ_e on edge features m_{ij} , which are summed into node features m_i used to update the hidden embedding h_i :

$$m_{ij} = \phi_e(h_i^l, h_j^l, a_{ij}) \quad (10)$$

$$m_i = \sum_{j \in \mathcal{N}(i)} m_{ij} \quad (11)$$

$$h_i^{l+1} = \phi_h(h_i^l, m_i) \quad (12)$$

Each message passing step (Eq. 12) is followed by a dense layer, a SiLU activation function, and another dense layer, which is added to the embedding and is repeated for n_{MP} steps.

Following the iterative message passing, the atom-wise features undergo further refinement where the output of two dense layers are combined using their tensor product (Eq. 7). The transformation of features to the desired output involves a dense projection which passes

the hidden state to a feed-forward neural network with a feature size of n_{DC} per atom. The `hardtanh` activation function scaled by a constant was used to limit the displacements of the distributed charges. The scaling factor used was 0.175 Å to limit displacements to no more than 0.3 Å away from the atomic centers although this hyperparameter may be adjusted.

The displacements of the distributed charges are obtained from the $\ell_p = 1_-$ features, while the $\ell_p = 0_+$ (scalar) features are input into a final dense layer (with an element specific bias) before the final readout step where n_{DC} distributed monopoles for each atom are obtained. Here the subscript denotes the parity of the feature, indicating the sign of the feature under inversion (e.g., $\ell_p = 1_-$ denotes the odd parity features which change sign under inversion). The final position of each distributed charge, $\boldsymbol{\delta}$, is the sum of the atom's position \mathbf{R} and the displacement vector obtained in the final readout \mathbf{r} .

Aside from rotational equivariance, the conservation of charge in an isolated system is another physical law that needs to be captured by the model. The correct total charge of the molecule, Z , may be fixed by subtracting the mean predicted charge per n_{DC} charges from the average charge per atom and adding the average remaining charge $\langle q \rangle$ to each of the charges

$$\langle q \rangle = \frac{Z}{N_{\text{atoms}}} - \frac{1}{n_{\text{DC}}} \sum_i^{n_{\text{DC}}} q_i \quad (13)$$

This transformation is applied after training, and in the read out of the validation loss. Empirically,^{37,41,52} including this constraint in the loss function has been shown to hinder training by slowing convergence and leading to models with larger errors. Penalizing the total molecular charge is more stable and to be preferred. The regularization of Eq. 13 can be applied during inference if required.

The loss function includes terms relating the root-mean-squared error of the electrostatic

potential evaluated on the grid, RMSE_{ESP} , between the reference molecular ESP_{ref} obtained from quantum chemical calculations and the ESP generated by the distributed charge model. The distributed charges are described by $\boldsymbol{\delta}$ (a vector consisting of a position and charge) evaluated over N_{grid} grid points \mathbf{y}_i , where the model ESP is calculated as the sum of the Coulomb interactions between each (distributed) charge and a probe charge of $1e$.

$$\text{RMSE}_{\text{ESP}}(\boldsymbol{\delta}) := \sqrt{\frac{1}{N_{\text{grid}}} \sum_{i=1}^{N_{\text{grid}}} [\text{ESP}_{\text{ref.}}(\mathbf{y}_i) - \text{ESP}_{\text{model}}(\mathbf{y}_i, \boldsymbol{\delta})]^2} \quad (14)$$

An additional (optional) term in the loss function corrects the molecular dipole moment generated by the distributed charges ($\mathbf{D}_{\text{DC}} = \sum_{i=0}^{N_{\text{atoms}}} q_{\text{DC},i}(\mathbf{R}_{\text{CoM}} - \boldsymbol{\delta}_{\text{DC},i})$), weighted by w_{D} is included in the loss function (Eq. 15):

$$\mathcal{L} = w_{\text{ESP}} \cdot \text{RMSE}_{\text{ESP}} + w_{\text{q}} \cdot \frac{1}{N_{\text{atoms}}} \sum_{i=0}^{N_{\text{atoms}}} \left(M_{\text{ref},i}^0 - \sum_{j=0}^{n_{\text{DC}}} M_{i,j}^0 \right)^2 + w_{\text{D}} \cdot \frac{1}{3} \sum_{\alpha=\{x,y,z\}} (D_{\text{ref},\alpha} - D_{\text{DC},\alpha})^2 \quad (15)$$

The mean absolute error between the MBIS monopoles and the per-atom sum of the distributed charges, weighted by w_{q} is also included. This term ensures that the distributed charges are able to reproduce the MBIS monopoles, however, any baseline charge assignment scheme can be used. Regularizing the sum of atomic charges to match the MBIS monopoles is an additional constraint also used in methods such as RESP,^{1,59} which uses an L_2 penalty to enforce consistent atomic charges even on buried atoms (i.e. no accessible volume or grid points associated with said atom), as ESP fitting is ill-posed in this case.

For vectorial quantities, such as molecular dipole vectors \mathbf{D} and forces \mathbf{F} , the average per-component RMSE and MAE were used and reported in the loss functions and results, respectively. The MBIS molecular dipole is calculated as $\mathbf{D}_{\text{MBIS}} = \sum_{i=0}^{N_{\text{atoms}}} q_i(\mathbf{R}_{\text{CoM}} - \mathbf{R}_i) + \sum_{i=0}^{N_{\text{atoms}}} \mathbf{M}_i^1$ where \mathbf{M}_i^1 is the atom-centered dipole moment on atom i obtained from the MBIS multipole expansion.

2.3 Data Generation

Training data compositions split tests into two main streams: (1) *conformational space*, where model a parametrizes electrostatics for many conformations of a single molecule, and (2) *chemical space*, where the model learns a shared electrostatic representation for a variety of molecules.

For models covering *conformational space*, 10,000 conformers were generated for carbon dioxide enumerating 100^3 combinations of the two CO bond lengths ($1.0 < r < 1.80 \text{ \AA}$) and OCO angle ($120^\circ < \theta < 180^\circ$) in a Z-matrix representation. Calculations were performed in Molpro⁶⁰ at the MP2/aug-cc-pVTZ level of theory with density fitting (using default parameters unless otherwise specified). Small perturbations (uniform random noise $\leq 0.01 \text{ \AA}$) was added to prevent redundancy in the dataset. All coefficients of the relaxed wavefunction were saved in the Molden format for further analysis in Multiwavefn,⁶¹ where ADCH, Becke, CHELPG, CM5, Hirshfeld, MBIS, MK, and VDD atom centered charges were obtained. Further, the MBIS multipole expansion ($\ell \leq 4$) was also derived. Training used the standard training/validation/testing splits (8:1:1).

For models covering *chemical space*, the QM9 database was employed.⁶² Data were split into three non-overlapping training/validation sets based on the order of molecules in the GDB dataset.⁶³ A total of 126900 molecules from QM9⁶² were split into three folds of 40000 structures each, and an additional holdout set of 6900 remaining structures was kept for testing. These structures were split based on their order in QM9 (i.e. based on the number of atoms): the training and test set contained molecules with 1 to 8 and 8 to 9 heavy atoms, respectively. QM9 consists of molecules containing carbon, hydrogen, oxygen and fluorine, up to nine heavy atoms. This introduced a sampling bias due to the upstream graph enumeration algorithm,

leading to chemically similar structures within individual splits. Training set sizes of 8k, 16k, and 32k molecules were used to benchmark and, in particular, learning curves, each with a constant validation set size of 8k structures. These models were trained for 500 epochs with a batch size of 16 and a learning rate of $1 \cdot 10^{-4}$. Final models were trained on 64k structures for 10000 epochs or until the validation loss of the models converged, using an 8k validation set and 6.9k molecules held out for testing. Molecular similarity was evaluated using the Tanimoto coefficient computed in RDKit,⁶⁴ based on two-hop Morgan fingerprints (1024 bits). TMAP projections⁶⁵ were generated using the MHFP encoder⁶⁶ to visualize molecular space coverage.

Analysis of the dataset based on the SMILES string deposited in the original QM9 dataset was performed using RDKit⁶⁴ (version 2023.5) and TMAP,⁶⁵ see Figure 9. As is typical when working with QM9,^{52,67–69} structures that failed simple consistency checks were removed, namely molecules with energies that were poorly converged or molecules that decomposed during optimization. For a given molecule, the energy was converged at the PBE0/def2-TZVP level of theory using PSI4,⁷⁰ and the wavefunction was analyzed, from which MBIS multipoles²¹ up to $\ell = 2$ and the electrostatic potential (evaluated on up to 3200 grid points) were obtained. Grid points were sampled on a regular grid generated by increasing the bounding box of the molecule by $\pm 3.0 \text{ \AA}$ along every direction, sampling 15 points along each axis. The effect of this relatively coarse grid was explored later. As the electrostatic potential distorts close to atomic nuclei due to charge penetration effects, a careful selection of grid points is important. Different grid point sampling methods were explored: an element-independent minimum distance cutoff of 1.7 \AA (i.e., $1 \times r_{\text{vdw}}$, the vdW radius of the largest atom, i.e., carbon), and element-dependent minimum distance cutoffs of $1.4 \times r_{\text{vdw}}$. Due to this sampling scheme, larger molecules typically featured a lower density of grid points.

Alternative examples of training data with mixed radial and angular grids were also explored. Specifically, the same grids as used in the RESP method were tested, *post-hoc* and not used in

any data in the main manuscript; however, the performance was seemingly improved, based on the quality of the dipole moment prediction. These observations are analogous to the long-range Coulomb interaction problem, which (famously) converges differently depending on how the long-range interaction pairs are selected.⁷¹

To assess robustness beyond the training setup, the ESP was evaluated on a finer grid and at a different level of theory. To evaluate the model’s ability to extrapolate, reference ESP data was computed at a different level of theory (MP2/6-31G(d,p)) using Gaussian16,⁷² in contrast to the DFT-level ESPs used for training. Further, ESP predictions were compared to a roughly ten-fold finer reference ESP grid than was used during training. The grid was partitioned into three regimes based on the ratio of the separation distance versus van der Waals radii (r/r_{vdw}): close- ($1.20 < r/r_{\text{vdw}} < 1.66$) , mid- ($1.66 < r/r_{\text{vdw}} < 2.20$) , and far-range ($2.20 < r/r_{\text{vdw}}$) regions relative to the molecular surface (see Table 4). This ensures a fair assessment of the transferability of the approach across different levels of theory and grid densities, which is desirable when employing these models in force-field fitting to alternative reference data.

For pretraining on chemical space, additional transfer learning (TL) experiments were performed outside the scope of the QM9 dataset which is restricted to equilibrium structures. Here, coordinates of 2040 random, neutral dipeptides sampled from gas-phase MD simulations at 500 K using were obtained from the SPICE dataset described by Eastman and coworkers.⁷³ Calculations as described above were performed to obtain the ESPs and molecular dipole moments.

2.4 Model Training

The DCM-net models were configured with the following hyperparameters: two message passing iterations, a cutoff radius of 4.0 Å (used to define graph edges), and a feature

size of 16, and 8 radial basis functions. Each feature was expanded up to $\ell = 2$. These hyperparameters were kept relatively small for speed of training and to aid against overfitting; however, increasing the feature size and number of radial basis functions appears to improve performance, and can likely be increased without significant drawbacks. Optimization of the NN was performed using the ADAM optimizer⁷⁴ ($\beta_1 = 0.9$, $\beta_2 = 0.999$, $\epsilon = 10^{-8}$) as implemented in the Optax library,⁵⁷ with a batch size of one. The loss function (Eq. 15) was weighted to balance the ESP and charge predictions. Specifically, the weight on the electrostatic potential term, $w_{\text{ESP}} = 10^5$ Hartree/e. This choice resulted in ESP and dipole contributions of comparable magnitude during training, when the weight for the atomic charges was $w_q = 1.0$ e. Initial experiments used an exponentially decaying learning rate (from $1 \cdot 10^{-3}$ to $1 \cdot 10^{-5}$) and gradient clipping (global norm, clip norm = 1),⁷⁵ with the objective of minimizing the squared error in the MBIS-derived monopoles and ESP (see Eq. 15). Learning curves from these models were used to validate the implementation (Figure 10, more details are provided in the SI). This weighting term was typically 1-2 orders of magnitude larger for the ESP than the total charge and molecular dipole terms. Charge weights $w_q = 1.0$ e ensured a correct first moment of the ESP to within 0.001 electron charge units, although training on datasets containing molecules with a non-zero net charge may require larger weights.

When pretraining on chemical space (QM9) and transferring to the dipeptide dataset, all Ala₂ and Gly₂ structures (63 conformers) were deposited in the test set to prevent any data leakage and to better justify the transferability of this approach. The remaining structures were used in the training and validation sets (1900 and 77, respectively). As in previous TL-studies,^{76,77} the learning rate was decreased by a factor of 100 to 2.5e-07, and all parameters of the model were optimized over 1000 steps of transfer learning.

3 Results and Discussion

DCM-net was evaluated along three axes: (1) practical generation of minimal charge models, (2) ESP accuracy versus MBIS multipoles, and (3) TL to out-of-distribution molecules. First, parametrization of conformational space is presented, and the motion the individual DCM-charges as a function of time and the symmetry of the models is investigated. Following this, an analysis of the accuracy of the model is provided in comparison to density derived atomistic multipole expansions obtained from MBIS, as well as a discussion on the training dynamics and model validation using the learning curves. As a proof-of-concept, minimal distributed charges are generated for a single molecules (Fluoro-Benzene, FBz) which can be readily used in MD simulations in packages such as CHARMM.⁷⁸ Finally, the capability for applying these models in a TL-setting is investigated.

3.1 Conformational Space: CO₂ and Rotational Equivariance

To probe how the model represents conformational variability in a symmetry-sensitive system, carbon dioxide (CO₂) is considered. In order to run dynamics, a message passing neural network as described previously³⁸ was used to predict energies, forces and dipole moments via atom centered fluctuating charges. Since the loss function, Eq. 15, includes a weighted atomic charge penalty, it is possible to couple the two models during training by using the learned PhysNet atomic charges as the reference atomic monopoles M_{ref}^0 in DCM-net.

Using the fitted potential energy surface, dynamics simulations were run. For this demonstration, random initial velocities were assigned at 300 K and positions were updated using a 0.5 fs time step. Figure 3 shows the dynamics of the DCM-net $n_{\text{DC}} = 2$ representation as a function of the bond lengths r_a , r_b and the internal angle θ . The distributed charges associated with each atom respond smoothly to distortions away from linearity, with displacements occurring

primarily along the molecular z axis, which is aligned with the C–O bonds, see Figure 3 panels a, b, c, and f. As the molecule approaches the symmetric configuration ($\theta = 180^\circ$), these displacements vanish and the charge magnitudes relax toward their mean values, consistent with the restoration of inversion symmetry. In addition to longitudinal motion, small but systematic displacements of the carbon-centered distributed charges are observed along the transverse x direction. These transverse shifts are coupled to changes in bond length and provide a mechanism for modulating the electrostatic potential without introducing spurious dipole moments in the linear limit. This behavior highlights how the model encodes internal polarization effects through geometry-dependent charge rearrangements while preserving the correct symmetry constraints. The resultant models are qualitatively similar to fluctuating distributed charge models described previously, despite differing in the fitting approach.^{79,80} The learned displacements are smaller for DCM-net, since the magnitude of the charges is allowed to fluctuate unlike approaches such the kernel-based minimal distributed charge model.

In the context of a small molecule potential, it is interesting to compare the performance of an equivariant (EQV) model versus a non-equivariant (NEQV) model. A shared parameter budget of 500,000 was applied to attempt a fair comparison; however, the results are arguably qualitative. Table 1 reports test-set errors for energies, forces, dipole moments, and electrostatic potentials after 1000 steps of training. The EQV model yields lower mean absolute errors for energies, forces, and dipoles compared to the NEQV model, along with reduced variability across independent training runs. Despite these marginal improvements, the performance of the models was comparable. Interestingly, the ESP errors were smaller for the NEQV model than the EQV model (2.59 versus 2.48 (kcal/mol)/ e) on the hold-out test set. Seemingly large errors in Table 1 are related to the highly non-equilibrium dataset which covers a range over 100 kcal/mol in energy. Nevertheless, it is worthwhile to note that for such small molecules kernel-based methods are often preferable if accuracy in the representation of the energies is sought.^{81,82}

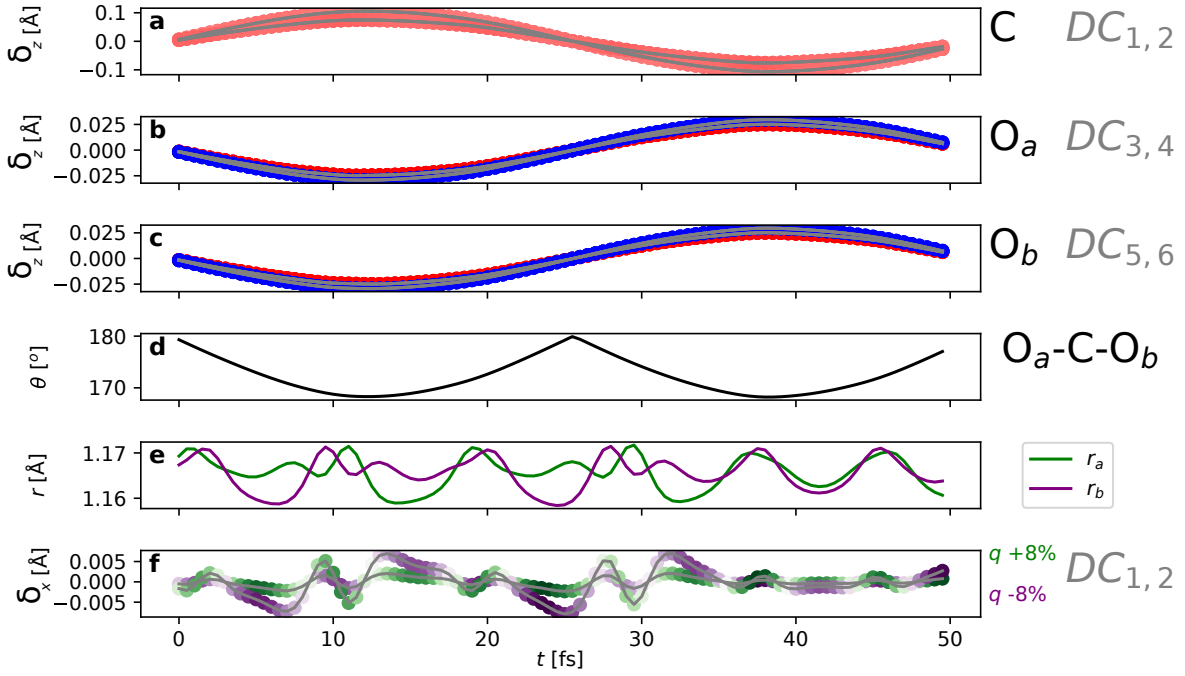


Figure 3: *Conformational space*: Dynamics of the DCM-net/PhysNet two charge model of CO₂ (a-c) Components of displacements for six distributed charges δ , labeled on the right hand side DC_{1-6} , coupled with (d) the internal angle θ , shown along the z axis which is aligned with bonds (e) r_a and r_b . (f) Small displacements along the x axis for the central carbon atom distributed charges ($DC_{1,2}$), and their magnitude q , couples the electrostatic potential to changes in bond length. For the symmetric case ($\theta = 180^\circ$), displacements approach 0.0 Å, and charges q approach their mean value.

Table 1: *Conformational space*: CO₂. Test Set MAE for energies E , forces \mathbf{F} , dipole moments \mathbf{D} and electrostatic potential RMSEs ΔESP , comparing (non)equivariant, (N)EQV, models. Uncertainties correspond to the standard deviation over three random trials. Large errors in the energy are related to the presence of outlier high-energy structures, as over 100 kcal/mol is covered in the dataset.

	E [kcal/mol]	\mathbf{F} [(kcal/mol)/Å]	\mathbf{D} [D]	ΔESP [(kcal/mol)/ e]
EQV	1.70 ± 1.48	0.305 ± 0.19	0.122 ± 0.05	2.59 ± 0.01
NEQV	1.97 ± 1.64	0.375 ± 0.25	0.127 ± 0.05	2.48 ± 0.02

This distinction becomes evident when explicit symmetry consistency tests, such as random rotations and translations, are applied. Table 2 summarizes rotational and translational errors in dipole moments and electrostatic potentials under random rigid-body transformations. The EQV model exhibits errors close to numerical precision, confirming exact rotational and translational equivariance by construction. In contrast, the NEQV model shows substantial rotational errors. Particularly, for the electrostatic potential, since distributed charges are predicted in 3D space, without rotational equivariance or averaging through data augmentation, the variance in errors were roughly 90% on the test set. Such large variations after applied rotations are explained by the entire dataset containing structures aligned to the principle molecular axes.

Table 2: *Conformational space*: CO_2 . Rotational and translational variations for dipole moments \mathbf{D} [D] and electrostatic potential RMSEs ΔESP [(kcal/mol)/ e)] evaluated on the test set, comparing (non)equivariant, (N)EQV, models. Rotations and translations were sampled uniformly at random.

	$\Delta\mathbf{D}_{\text{rot}}$	$\Delta\text{ESP}_{\text{rot}}$	$\Delta\mathbf{D}_{\text{trans}}$	$\Delta\text{ESP}_{\text{trans}}$
EQV	4.04×10^{-4}	0.02	6.74×10^{-6}	2.26×10^{-4}
NEQV	5.84×10^{-2}	2.26	3.52×10^{-5}	3.06×10^{-3}

Across conformational space, these results demonstrate that enforcing equivariance provides geometrically consistent, and therefore physically meaningful, electrostatic representations - providing a basis for more complex models attempting to learn shared representations across chemical space.

3.2 Chemical Space: Accuracy of the Electrostatic Potential

After validating DCM-net for an ensemble of structures of single molecule in the gas phase, an application across the chemical space covered by the QM9 data set is discussed next. For this, DCM-net was trained as described in the Methods section.

The distributed charge positions predicted by DCM-net are able to reduce the average RMSE error in the ESP in comparison to fitted MBIS monopoles, and reach similar accuracy of the fitted multipole expansion up to $l = 1$ when more than $n_{\text{DC}} > 2$ are predicted (Table 3); however, the accuracy for the model with $n_{\text{DC}} > 4$ is slightly worse than the MBIS expansion up to atomic quadrupoles (0.6 versus 0.5 (kcal/mol)/ e on the test set). Figure 4A reports the distribution of ESP errors for increasing multipole ranks/number of distributed charges per atom for all molecules in the test set. The shape of the error distributions for multipole- and distributed charge-based ESPs are comparable, indicating a uniform improvement for the test set as the number of distributed charges increases. If the error distributions associated with the predicted distributed charges were skewed with heavy tails it may suggest that the learned

distributed charge representations were biased towards certain types of molecules; however, the comparable improvements in the error distributions suggest the DCM-net approach is transferable (at least within the chemical space of QM9) and increasing the number of distributed charges provides benefits almost on par with increasing the rank of the multipole expansion.

The sum of the distributed charges per atom closely matches the target MBIS monopoles (Table 3) implying that the improvement is a result of the anisotropic nature of the off-center charges and not due to the model ‘cheating’ by assigning physically unrealistic charges to buried atoms (i.e. no accessible volume or grid points evaluated by the loss function for those atoms). This assessment is further supported by comparing the distributions of such charges obtained using MBIS and DCM-net, as well as a general fixed charge force field such as CGenFF (see SI, Figure 11). By applying this constraint, predictions from DCM-net can be converted to an equivalent atom-centered model on an atom-by-atom basis to create minimal models with acceptable accuracy and low computational complexity.

To analyze for which chemically relevant situations and features using distributed charges is most beneficial, each ESP-grid point was associated with the atom closest to it in space: either (1) by element (Figure 4B and C), or (2) by CGenFF atom-type (Tables 5 and 6). Although the ESP at a certain grid point contains contributions from the entire molecule, the closest atom/distributed charge is expected to have the largest impact on the associated error. Additionally, since atoms such as carbon are usually buried and occluded by hydrogen atoms, the relative errors for different elements should not be compared directly, and a comparison between different electrostatic models is more consistent.^{2,83} For atom-centered multipoles, the average quality of the ESP around carbon and nitrogen atoms is only significantly improved with the addition of atom centered quadrupoles as many heteroaromatic rings present in the test set are expected to have significant quadrupole contributions to the ESP related to

the presence of π -bonds.^{2,17} In contrast, distributed charges appear to be an efficient way of representing such anisotropic charge distributions as even the $n_{DC} = 2$ model reaches quadrupolar accuracy around these atomic centers.

For local environments around fluorine atoms, the improvement gained for $n_{DC} > 2$ is much smaller in comparison to increasing the rank of the multipole expansion. In contrast, the addition of atomic quadrupoles nearly halves the median RMSE_{ESP}. For oxygen atoms, adding atom centered dipoles reduces the median RMSE_{ESP} from ~ 1.1 to ~ 0.6 (kcal/mol)/e. This is related to the improved description of hydroxy (-OH) groups which have a significant dipolar character. In contrast, improvement gained from a model with $n_{DC} = 2$ instead is slightly smaller (from ~ 1.1 to ~ 0.8 (kcal/mol)/e). The performance of the atom-centered dipole model is reached with $n_{DC} = 3$, whereas $n_{DC} = 4$ does not provide further improvements.

The same analysis was repeated by separating the grid points into a larger number of classes based on their proximity to different CGenFF atom types (see SI, Tables 5 and 6). Here, only molecules in the test set with available CGenFF atom types were analyzed and the amount of data for each class is significantly lower and considering the limitations mentioned above it is more difficult to make well-grounded conclusions as to which atom types benefit the most from improved electrostatic representations. As expected, increasing the rank of the MBIS multipole expansion monotonically decreases the errors associated with all atom types (Table 5). In contrast, using this ad-hoc partitioning scheme reveals that the learned distributed charge representations only provide a small improvement in comparison to MBIS monopoles for certain atom types and, furthermore, the improvement gain from increasing the number of distributed charges per atom is not monotonic in all cases likely due to the stochastic nature of training and the non-unique nature of the fitting problem resulting in a

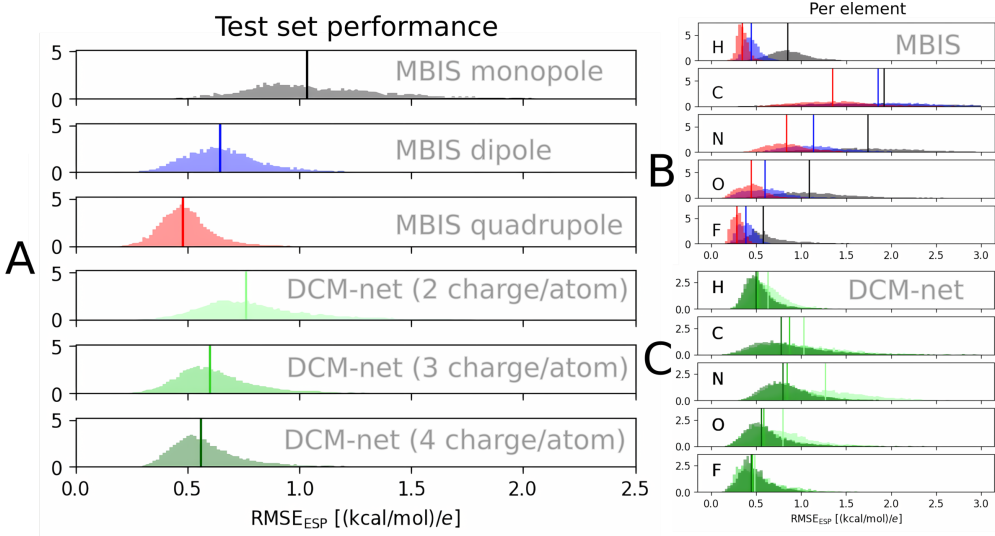


Figure 4: *Chemical space*: QM9 (A) Distribution of RMSE_{ESP} values (difference between the model and reference ESP) for the entire hold-out (test) set, (B) contributions based on individual elements contributions for multipoles and (C) DCM-net. The normalized probability density is shown on the *y*-axis. Atom centered multipole expansions up to monopole (black), dipole (blue) and quadrupole (red) are shown along with the two-, three-, and four-charge-per atom models shown in pale green, green and dark green, respectively. The median of the distributions are shown with vertical lines. Note the change in height of the distributions for the DCM-net models due to fatter tails in the distribution.

glassy loss landscape. Unsurprisingly, given the chemical diversity of the four splits in the SI (Figure 9), chemical biases were observed in training across splits.

Figure 5 shows examples of the positions of the predicted distributed charges, and grid points of the error surface with errors higher than 75% of the mean absolute error obtained with fitted atom-centered point charges. The error is expected to be larger at points closest to the molecule where the potential is large; grid points further away with significant errors ($\geq 75\%$ of the baseline error) point to regions where anisotropy can be improved. Strikingly, all distributed charge models reduce the error on grid points around the fluorine atom (shown in green, Figure 5A2-A4), which is expected to have pronounced anisotropic features in the ESP due to the σ -hole that is known to be difficult to capture with atom centered point charges alone.^{6-8,84} The location of grid points have implications seen in the predicted charge

magnitudes. For instance, for models trained on grid points closer than $1.4 \times r_{\text{vdw}}$ of the atoms (i.e. points where the ESP is influenced by charge penetration effects), the spatial distributions of grid points with high errors were typically larger, although the DCM-net models had lower overall RMSEs than the MBIS-fitted point charges. This demonstrates a bias towards close-range points of the ESP. After addressing the issue of the selection of the grid points on which to evaluate the ESP in the training data, e.g. by excluding close range point, the spatial distributions of errors were comparable to the MBIS-fitted point charges without any drawbacks to the overall accuracy of the ESP.

As for all deep-learning models, performance drops are expected when leaving the training distribution.⁸⁵⁻⁸⁷ One limitation of the machine learned distributed charges is the presence outliers in the of long-tails of the distribution. For some structures, the error in the ESP is significantly larger than that of the equivalent MBIS monopoles. An important consideration in the extrapolation capability of atomistic neural network models is the coverage of chemical in the training data space^{85,86} (see SI, Figure 9). The maximum Tanimoto similarity⁸⁸ of the 100 structures with highest error in the test was 0.4; compared to 0.5 for 100 structures with the lowest errors, which suggests that these outliers may be related to insufficient training examples for particular classes of molecules.

The mean absolute errors of the components of the molecular dipole moment for various models are given in Table 3. Although the $n_{\text{DC}} = 2$ model significantly reduces the error in the molecular dipole moment in comparison to MBIS monopoles (from 0.195 D to 0.123 D), the improvement saturates with increasing numbers of distributed charges per atom with the three and four charge models exhibiting only slight improvements (0.110 D and 0.105 D). These results are inline with previous atom centered point charge models such as PhysNet;³⁸ however, still behind that of atom centered multipoles³⁷ and naturally behind the performance of MBIS atomistic dipoles derived from wavefunction based densities so

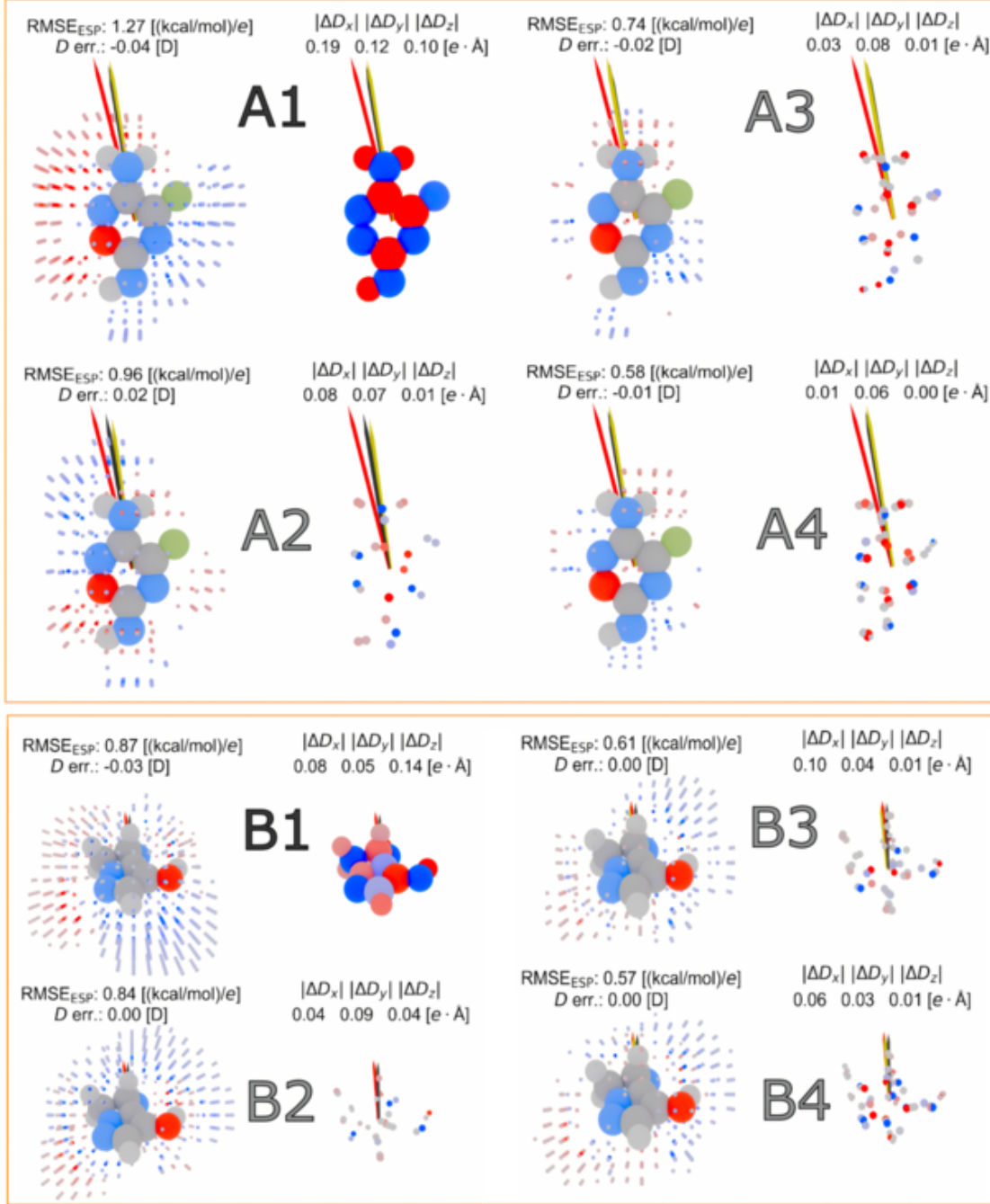


Figure 5: *Chemical space*: The spatial extent of the improvement introduced by DCM-net in comparison to MBIS point charges (note the color scale is qualitative; identifying regions of positive/negative errors and charge), for randomly selected test set examples labeled. Panel A ($\text{C}_3\text{H}_3\text{N}_4\text{OF}$) and panel B ($\text{C}_5\text{H}_7\text{N}_3\text{O}$), with (1, black) MBIS point charges, (2-4, gray) DCM-net predictions for $n_{\text{DC}} = 2, 3, 4$, respectively. On the left, grid points with greater than 75% of the absolute error for the monopole ESP. On the right, molecular dipole vectors (scaled by 4 \times for clarity) of (black) the ground truth, and of (red) the MBIS monopole and (yellow) DCM-net models. Errors, typically, decrease as the number of distributed charges per atom increases. Atoms are colored gray (carbon), white (hydrogen), red (oxygen), blue (nitrogen), and green (fluorine).

Table 3: *Chemical space*: Performance of the DCM-net models with n_{DC} distributed charges per atom, measured by $RMSE_{ESP}$ error with respect to the reference ESP, in comparison to MBIS multipoles. The average $RMSE$ of the ESP for the molecules in the test set $\langle RMSE_{ESP} \rangle$ values are in (kcal/mol)/ e . The mean absolute error between the sum of the DCM-net distributed charges per atom and MBIS $MAE_{l=0}$, $MAE_{l=0}$, is in elementary charge e , and the mean absolute error of the components of the molecular dipole moment, MAE_D , is given in Debye.

	$\langle RMSE_{ESP} \rangle$	$MAE_{l=0}$	MAE_D
$l = 0$	1.1	-	0.195
$l \leq 1$	0.7	-	0.001
$l \leq 2$	0.5	-	0.001
$n_{DC}=2$	0.8	0.004	0.123
$n_{DC}=3$	0.7	0.003	0.110
$n_{DC}=4$	0.6	0.003	0.105

naturally fit the data better.²¹ In contrast, the MBIS atomic dipoles are, by construction, functions of local atomic densities and are fit to reproduce the total dipole of the molecular wavefunction and as a result the associated errors are small (0.001 D). A significant advantage of using atomic dipoles is that unlike dipoles obtained from two off-center point charges, atom centered dipoles can simply be added together to obtain the molecular dipole moment since the two are both rank-1 tensors.

3.3 Generating Minimal Distributed Charge Models

The model’s ability to generate “minimal” distributed charge models was investigated. Fluorobenzene (Figure 6) was selected for this task, as the molecule was not included in the training set but is, importantly, still within the data distribution of QM9 (i.e. < 10 heavy atoms). The results are compared with a model obtained using a differential-evolution optimization scheme³² where 19 charges were selected as a viable trade-off between complexity and accuracy. Having established that DCM-net produces symmetry-consistent minimal models comparable to DE, the ESP accuracy against baselines from atom-centered multipoles

is assessed next. In this case, the model was obtained from $n_{DC} > 2$ per heavy atom, whereas hydrogen atoms were assigned one on-site charge. The model obtained from DCM-net was similar or slightly better than the model obtained from DE for all regions of the ESP, including maximum errors (Table 4).

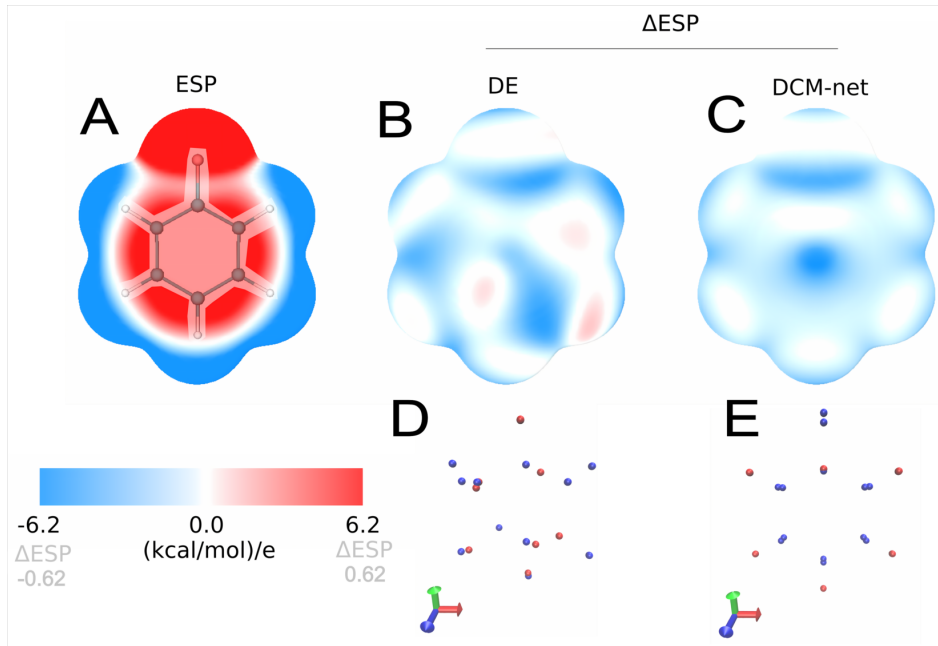


Figure 6: *Model building*: Fluorobenzene (F-Bz). The ground truth electrostatic potential surface of using a color map from -6.2 to $(6.2 \text{ kcal/mol})/e$, at an isodensity of 0.01 a.u., compared to the error surfaces from a 19 charge model generated by differential evolution (DE) and DCM-net ($n_{DC} = 2$), using a color map from -0.62 to 0.62 (10% of the original color scale). Both models achieve comparable accuracy (0.6 versus 0.5 $(\text{kcal/mol})/e$). F-Bz was not present in the training set and serves as a rigorous prediction test for DCM-net. The error surface of the equivariant model is consistent with the symmetry of the molecule.

The DCM-net model leverages the symmetry of the local molecular environment (due to message passing and the inclusion of rigorous equivariance), and as a result, the distributions of errors across the ESP surface are also symmetric. It is also possible to enforce symmetric charge positions based on the entire point group of the molecule; however, such high symmetry examples become less common for larger molecules. Leveraging the local symmetries of the atomic environments is clearly advantageous, as it leads to similar distributed charge positions for similar functional groups, without any requirements on the molecule global symmetry,

and can smoothly interpolate between similar molecules/conformations. Conformational averaging (i.e. finding charge distributions which are consistent across different molecular conformations) is done implicitly through the selection of the training data, allowing for the model to better generalize to new conformations. In contrast, the DE routine requires the optimization of the charge positions for each conformation. Given these advantages, a practical application of this model is in automated force field and topology builders.^{25,78,89–91}

Table 4: *Model building*: Fluorobenzene. Comparison of RMSE, Max Error, and Number of Points for two sets of data across different ranges. The grid points are selected based on r , the ratio of the distance divided by the vdW radii for the closest atom.

Range	DCM-net		DE		N_{grid}
	RMSE _{ESP}	max.	RMSE _{ESP}	max.	
Total	5.4e-01	12.8	6.2e-01	12.9	415153
Close ($1.20 < r < 1.66$)	1.1	12.8	1.2	12.9	90064
Mid-range ($1.66 < r < 2.20$)	2.3e-01	1.4	3.3e-01	1.5	152428
Far-range ($2.20 < r$)	7.5e-02	0.4	1.1e-01	0.6	172661

3.4 Transfer Learning to Non-Equilibrium Structures

Finally, generalization to flexible, protein-like motifs is considered by adapting the model trained in 3.2 on QM9 to a set of dipeptides via lightweight transfer learning. A strict training set containing unseen dipeptides (Ala_2 and Gly_2) was enforced to see if the information contained in QM9 and the remaining neutral dipeptides, would allow the model to generalize out of distribution. Transfer learning exploits mutual information between different tasks to speed-up training and to increase performance in downstream (usually orthogonal) tasks.^{76,77} Here, TL-predictions of the model based on QM-minimized structures to structures obtained from cruder molecular mechanics-based methods is investigated.

Training on structures from QM9 introduces a bias to (near) equilibrium conformations^{62,68} One meaningful test of the consistency of the model with respect to non-equilibrium conforma-

tions carried out was to take the SMILES representation of the molecule and recalculate the molecular geometry using RDKit’s standard (empirical) distance-geometry-based conformer generator.⁶⁴ These structures were typically tens of kcal/mol higher in energy than the geometries obtained from QM9, and contain molecules with substantially different distributions of bond lengths and angles present in QM9.

In this out-of-distribution regime, the ESP errors were generally larger than those of the fitted MBIS monopoles. These are not deficits of the model *per se*, since the data set can be adapted and the model can be retrained using a TL-strategy.^{76,77} The final average ESP error over the unseen structures was 0.6 (kcal/mol)/*e*, which is a 0.2 (kcal/mol)/*e* improvement over the MBIS monopoles (0.8 (kcal/mol)/*e*); and the MAE of the molecular dipole was 0.1314 D in comparison to 0.2552 D.

Modest improvements in comparison to fitted MBIS monopoles are consistent with the results in Table 3, and suggest that the $n_{DC} = 2$ model is not competitive with higher order multipolar expansions derived from atomic densities (bear in mind these are fit to reproduce the first three moments of the ESP), as the inclusion of atomistic dipoles with and without quadrupoles achieved 0.4 and 0.3 (kcal/mol)/*e* in the average RMSE of the ESP, and reached a MAE of 0.002 D across predictions of the molecular dipole moment. The weaker results on the dipole moment are due to (1) approximation errors due to using point charges (instead of atomistic dipoles) and (2) difficulties in training with multiple objectives and constraints in the loss function. Training iteratively between putting higher weights on either the dipole or ESP objectives, improved the final results slightly, as is observed when training models on energy and forces.⁵⁸ During transfer learning, the observed decrease in required training time and increase in accuracy constitute additional evidence that the features learned by the model are robust and transferable to a diverse set of molecular conformations or chemical systems.

4 Conclusions

Across tasks, DCM-net produces symmetry-consistent minimal models quickly and reduces ESP error relative to fitted MBIS monopoles, approaching dipole-level multipolar accuracy when two or more charges per atom are used, particular in regions with π -bonds and σ -holes. Equivariance through construction, as presented here, is ultimately a design choice and alternatives such as data augmentation are routinely employed.^{39,49} The approach outlined in the present work streamlines the generation of distributed charges with specified accuracy or complexity, depending on the chosen n_{DC} . These models can be introduced as rigid distributed point charges into empirical force fields and given a diverse training set, additional parameters can be optimized against a consistent charge model in a transferable fashion, allowing for the rapid development of force fields with anisotropic electrostatics. Furthermore, studies of models that include conformational sampling for the training data suggest that distributed charges can be used alongside machine learned potential energy surfaces to improve the description of polarization and electrostatics.

Acknowledgement

This work was supported by the Swiss National Science Foundation through grants 200020_219779 and 200021_215088 and the University of Basel.

Supporting Information Available

All data and computer codes for this work are available from the authors upon reasonable request. A demo of the DCM-net model is available as a Space on HuggingFace at <https://huggingface.co/spaces/EricBoi/DCMNet> which sources the publically available repository at <https://github.com/EricBoittier/dcmnet>. The core functionality for building the training datasets, as well as training and evaluating the combined DCM-net and PhysNet

model are available from the public repository at <https://github.com/EricBoittier/mmml.git>.

References

- (1) Bayly, C. I.; Cieplak, P.; Cornell, W.; Kollman, P. A. A well-behaved electrostatic potential based method using charge restraints for deriving atomic charges: the RESP model. *J. Phys. Chem.* **1993**, *97*, 10269–10280.
- (2) Stone, A. J. *The Theory of Intermolecular Forces*, 2nd ed.; Oxford University Press, 2013.
- (3) Murray, J. S.; Politzer, P. The Electrostatic Potential: An Overview. *WIREs Comput. Mol. Sci.* **2011**, *1*, 153–163.
- (4) Politzer, P.; Murray, J. S. The Fundamental Nature and Role of the Electrostatic Potential in Atoms and Molecules. *Theor. Chem. Acc.* **2002**, *108*, 134–142.
- (5) Suresh, C. H.; Remya, G. S.; Anjalikrishna, P. K. Molecular Electrostatic Potential Analysis: A Powerful Tool to Interpret and Predict Chemical Reactivity. *WIREs Comput. Mol. Sci.* **2022**, *12*, e1601.
- (6) Ibrahim, M. A. A. Molecular mechanical study of halogen bonding in drug discovery. *J. Chem. Theory Comput.* **2011**, *32*, 2564–2574.
- (7) Jorgensen, W. L.; Schyman, P. Treatment of halogen bonding in the OPLS-AA force field: application to potent anti-HIV agents. *J. Chem. Theory Comput.* **2012**, *8*, 3895–3901.
- (8) Yan, X. C.; Robertson, M. J.; Tirado-Rives, J.; Jorgensen, W. L. Improved Description of Sulfur Charge Anisotropy in OPLS Force Fields: Model Development and Parameterization. *J. Phys. Chem. B* **2017**, *121*, 6626–6636.

(9) Kolář, M.; Hobza, P. On Extension of the Current Biomolecular Empirical Force Field for the Description of Halogen Bonds. *J. Chem. Theory Comput.* **2012**, *8*, 1325–1333.

(10) Kramer, C.; Spinn, A.; Liedl, K. R. Charge Anisotropy: Where Atomic Multipoles Matter Most. *J. Chem. Theory Comput.* **2014**, *10*, 4488–4496.

(11) Kramer, C.; Gedeck, P.; Meuwly, M. Atomic multipoles: Electrostatic potential fit, local reference axis systems, and conformational dependence. *J. Comput. Chem.* **2012**, *33*, 1673–1688.

(12) Bereau, T.; Kramer, C.; Monnard, F. W.; Nogueira, E. S.; Ward, T. R.; Meuwly, M. Scoring Multipole Electrostatics in Condensed-Phase Atomistic Simulations. *J. Phys. Chem. B* **2013**, *117*, 5460–5471.

(13) Bereau, T.; Kramer, C.; Meuwly, M. Leveraging Symmetries of Static Atomic Multipole Electrostatics in Molecular Dynamics Simulations. *J. Chem. Theory Comput.* **2013**, *9*, 5450–5459.

(14) Faerman, C. H.; Price, S. L. A transferable distributed multipole model for the electrostatic interactions of peptides and amides. *J. Am. Chem. Soc.* **1990**, *112*, 4915–4926.

(15) Plattner, N.; Meuwly, M. The role of higher CO-multipole moments in understanding the dynamics of photodissociated carbonmonoxide in myoglobin. *Biophys. J.* **2008**, *94*, 2505–2515.

(16) Ponder, J. W.; Wu, C.; Ren, P.; Pande, V. S.; Chodera, J. D.; Schnieders, M. J.; Haque, I. et al. Current status of the AMOEBA polarizable force field. *J. Phys. Chem. B* **2010**, *114*, 2549–2564.

(17) Day, G. M.; Motherwell, W. D. S.; Jones, W. Beyond the Isotropic Atom Model in Crystal Structure Prediction of Rigid Molecules: Atomic Multipoles versus Point Charges. *Cryst. Growth Des.* **2005**, *5*, 1023–1033.

(18) Devereux, M.; Gresh, N.; Piquemal, J.-P.; Meuwly, M. A supervised fitting approach to force field parametrization with application to the SIBFA polarizable force field. *J. Comput. Chem.* **2014**, *35*, 1577–1591.

(19) Dykstra, C. E. Electrostatic Interaction Potentials in Molecular Force Fields. *Chem. Rev.* **1993**, *93*, 2339–2353.

(20) Heindel, J. P.; Kim, L.; Head-Gordon, M.; Head-Gordon, T. Completely Multipolar Model for Many-Body Water–Ion and Ion–Ion Interactions. *J. Phys. Chem. Lett.* **2025**, *16*, 975–984.

(21) Verstraelen, T.; Vandenbrande, S.; Heidar-Zadeh, F.; Vanduyfhuys, L.; Van Speybroeck, V.; Waroquier, M.; Ayers, P. W. Minimal Basis Iterative Stockholder: Atoms in Molecules for Force-Field Development. *J. Chem. Theory Comput.* **2016**, *12*, 3894–3912.

(22) Misquitta, A. J.; Stone, A. J.; Fazeli, F. Distributed Multipoles from a Robust Basis-Space Implementation of the Iterated Stockholder Atoms Procedure. *J. Chem. Theory Comput.* **2014**, *10*, 5405–5418.

(23) Weiner, S. J.; Kollman, P. A.; Case, D. A.; Singh, U. C.; Ghio, C.; Alagona, G.; Profeta, S. et al. A new force field for molecular mechanical simulation of nucleic acids and proteins. *J. Am. Chem. Soc.* **1984**, *106*, 765–784.

(24) Dixon, R. W.; Kollman, P. A. Advancing beyond the atom-centered model in additive and nonadditive molecular mechanics. *J. Comput. Chem.* **1997**, *18*, 1632–1646.

(25) Abraham, M.; Alekseenko, A.; Basov, V.; Bergh, C.; Briand, E.; Brown, A.; Doijade, M. et al. GROMACS 2024.2 Manual. 2024; <https://doi.org/10.5281/zenodo.11148638>.

(26) Devereux, M.; Raghunathan, S.; Fedorov, D. G.; Meuwly, M. A Novel, Computationally Efficient Multipolar Model Employing Distributed Charges for Molecular Dynamics Simulations. *J. Chem. Theory Comput.* **2014**, *10*, 4229–4241.

(27) Devereux, M.; Boittier, E. D.; Meuwly, M. Systematic improvement of empirical energy functions in the era of machine learning. *J. Comput. Chem.* **2024**, *45*, 1899–1913.

(28) Koch, U.; Popelier, P.; Stone, A. Conformational dependence of atomic multipole moments. *Chem. Phys. Lett.* **1995**, *238*, 253–260.

(29) Boittier, E. D.; Devereux, M.; Meuwly, M. Molecular Dynamics with Conformationally Dependent, Distributed Charges. *J. Chem. Theory Comput.* **2022**, *18*, 7544–7554.

(30) Boittier, E.; Töpfer, K.; Devereux, M.; Meuwly, M. Kernel-based Minimal Distributed Charges: A Conformationally Dependent ESP-Model for Molecular Simulations. **2024**, arXiv:2406.00513 [physics].

(31) Jakobsen, S.; Jensen, F. Systematic Improvement of Potential-Derived Atomic Multipoles and Redundancy of the Electrostatic Parameter Space. *J. Chem. Theory Comput.* **2014**, *10*, 5493–5504.

(32) Unke, O. T.; Devereux, M.; Meuwly, M. Minimal distributed charges: Multipolar quality at the cost of point charge electrostatics. *J. Chem. Phys.* **2017**, *147*, 161712.

(33) Warshel, A.; Kato, M.; Pisliakov, A. V. Polarizable Force Fields: History, Test Cases, and Prospects. *J. Chem. Theory Comput.* **2007**, *3*, 2034–2045.

(34) Bereau, T.; Andrienko, D.; von Lilienfeld, O. A. Transferable Atomic Multipole Machine Learning Models for Small Organic Molecules. *J. Chem. Theory Comput.* **2015**, *11*, 3225–3233.

(35) Zare, R. N. *Angular Momentum: Understanding Spatial Aspects in Chemistry and Physics*; John Wiley & Sons, 1988.

(36) Brink, D. M.; Satchler, G. R. *Angular Momentum*, 3rd ed.; Oxford University Press, 1993.

(37) Thürlemann, M.; Bösel, L.; Riniker, S. Learning Atomic Multipoles: Prediction of the Electrostatic Potential with Equivariant Graph Neural Networks. *J. Chem. Theory Comput.* **2022**, *18*, 1701–1710.

(38) Unke, O. T.; Meuwly, M. PhysNet: A Neural Network for Predicting Energies, Forces, Dipole Moments, and Partial Charges. *J. Chem. Theory Comput.* **2019**, *15*, 3678–3693.

(39) Bronstein, M. M.; Bruna, J.; LeCun, Y.; Szlam, A.; Vandergheynst, P. Geometric deep learning: going beyond Euclidean data. *IEEE Signal Process. Mag.* **2017**, *34*, 18–42, arXiv:1611.08097 [cs].

(40) Duval, A.; Mathis, S. V.; Joshi, C. K.; Schmidt, V.; Miret, S.; Malliaros, F. D.; Cohen, T. et al. A Hitchhiker’s Guide to Geometric GNNs for 3D Atomic Systems. **2024**, arXiv:2312.07511 [cs, q-bio, stat].

(41) Schütt, K.; Unke, O.; Gastegger, M. Equivariant message passing for the prediction of tensorial properties and molecular spectra. Proceedings of the 38th International Conference on Machine Learning. 2021; p 9377–9388.

(42) Batatia, I.; Batzner, S.; Kovács, D. P.; Musaelian, A.; Simm, G. N. C.; Drautz, R.; Ortner, C. et al. The Design Space of $E(3)$ -Equivariant Atom-Centered Interatomic Potentials. **2022**, arXiv:2205.06643 [cond-mat, physics:physics, stat].

(43) Brandstetter, J.; Hesselink, R.; van der Pol, E.; Bekkers, E. J.; Welling, M. Geometric and Physical Quantities Improve $E(3)$ Equivariant Message Passing. **2022**, arXiv:2110.02905 [cs, stat].

(44) Batatia, I.; Kovács, D. P.; Simm, G. N. C.; Ortner, C.; Csányi, G. MACE: Higher Order Equivariant Message Passing Neural Networks for Fast and Accurate Force Fields. **2023**, arXiv:2206.07697 [cond-mat, physics:physics, stat].

(45) Frank, J. T.; Unke, O. T. So3krates: Equivariant attention for interactions on arbitrary length-scales in molecular systems. **2023**, arXiv:2205.14276 [cond-mat, physics:physics].

(46) Simeon, G.; de Fabritiis, G. TensorNet: Cartesian Tensor Representations for Efficient Learning of Molecular Potentials. **2023**, arXiv:2306.06482 [physics].

(47) Sun, J.; Cheng, L.; Miller, I., Thomas F. Molecular dipole moment learning via rotationally equivariant derivative kernels in molecular-orbital-based machine learning. *J. Chem. Phys.* **2022**, *157*, 104109.

(48) Kumar, A.; Pandey, P.; Chatterjee, P.; MacKerell, A. D. Deep Neural Network Model to Predict the Electrostatic Parameters in the Polarizable Classical Drude Oscillator Force Field. *J. Chem. Theory Comput.* **2022**, *18*, 1711–1725.

(49) Pozdnyakov, S. N.; Ceriotti, M. Smooth, exact rotational symmetrization for deep learning on point clouds. **2023**, arXiv:2305.19302 [cond-mat, physics:physics].

(50) Wang, Y.; Elhag, A. A.; Jaity, N.; Susskind, J. M.; Bautista, M. A. Swallowing the Bitter Pill: Simplified Scalable Conformer Generation. **2024**,

(51) Glick, Z. L.; Koutsoukas, A.; Cheney, D. L.; Sherrill, C. D. Cartesian message passing neural networks for directional properties: Fast and transferable atomic multipoles. *J. Chem. Phys.* **2021**, *154*, 224103.

(52) Unke, O.; Bogojeski, M.; Gastegger, M.; Geiger, M.; Smidt, T.; Müller, K.-R. SE(3)-equivariant prediction of molecular wavefunctions and electronic densities. Advances in Neural Information Processing Systems. 2021; p 14434–14447.

(53) Koker, T.; Quigley, K.; Taw, E.; Tibbetts, K.; Li, L. Higher-order equivariant neural networks for charge density prediction in materials. *npj Comput. Mater.* **2024**, *10*, 1–10.

(54) Li, C.; Sharir, O.; Yuan, S.; Chan, G. K. Image Super-resolution Inspired Electron Density Prediction. **2024**, arXiv:2402.12335 [physics].

(55) Jackson, J. D. *Classical electrodynamics*, 3rd ed.; John Wiley & Sons, 1999.

(56) Buckingham, A. D.; Disch, R. L.; Dunmur, D. A. Quadrupole Moments of Some Simple Molecules. *J. Am. Chem. Soc.* **1968**, *90*, 3104–3107.

(57) Babuschkin, I.; Baumli, K.; Bell, A.; Bhupatiraju, S.; Bruce, J.; Buchlovsky, P.; Budden, D. et al. The DeepMind JAX Ecosystem. 2020; <http://github.com/google-deepmind>.

(58) Unke, O. T.; Maennel, H. E3x: E(3)-Equivariant Deep Learning Made Easy. **2024**, arXiv:2401.07595 [physics].

(59) Singh, U. C.; Kollman, P. A. An approach to computing electrostatic charges for molecules. *J. Comput. Chem.* **1984**, *5*, 129–145.

(60) Werner, H.-J.; Knowles, P. J.; Manby, F. R.; Black, J. A.; Doll, K.; Heßelmann, A.; Kats, D. et al. The Molpro quantum chemistry package. *J. Chem. Phys.* **2020**, *152*, 144107.

(61) Lu, T. A Comprehensive Electron Wavefunction Analysis Toolbox for Chemists, Multi-wfn. *161*, 082503.

(62) Ramakrishnan, R.; Dral, P. O.; Rupp, M.; von Lilienfeld, O. A. Quantum chemistry structures and properties of 134 kilo molecules. *Sci. Data* **2014**, *1*, 140022.

(63) Ruddigkeit, L.; van Deursen, R.; Blum, L. C.; Reymond, J.-L. Enumeration of 166 Billion Organic Small Molecules in the Chemical Universe Database GDB-17. *J. Chem. Inf. Model.* **2012**, *52*, 2864–2875.

(64) Landrum, G.; Tosco, P.; Kelley, B.; Ric; Cosgrove, D.; sriniker; Vianello, R. et al. rdkit/rdkit: Release_2023.09.5. 2024; <https://doi.org/10.5281/zenodo.10633624>.

(65) Probst, D.; Reymond, J.-L. Visualization of very large high-dimensional data sets as minimum spanning trees. *J. Chem. Inf. Model.* **2020**, *12*, 12.

(66) Probst, D.; Reymond, J.-L. A probabilistic molecular fingerprint for big data settings. *J. Cheminf.* **2018**, *10*, 66.

(67) Unke, O. T.; Meuwly, M. A reactive, scalable, and transferable model for molecular energies from a neural network approach based on local information. *J. Chem. Phys.* **2018**, *148*, 241708.

(68) Kim, H.; Park, J. Y.; Choi, S. Energy refinement and analysis of structures in the QM9 database via a highly accurate quantum chemical method. *Sci. Data* **2019**, *6*, 109.

(69) Weinreich, J.; Browning, N. J.; von Lilienfeld, O. A. Machine learning of free energies in chemical compound space using ensemble representations: Reaching experimental uncertainty for solvation. *J. Chem. Phys.* **2021**, *154*, 134113.

(70) Smith, D. G. A.; Burns, L. A.; Simmonett, A. C.; Parrish, R. M.; Schieber, M. C.; Galvelis, R.; Kraus, P. et al. PSI4 1.4: Open-source software for high-throughput quantum chemistry. *J. Chem. Phys.* **2020**, *152*, 184108.

(71) Kolafa, J.; Perram, J. W. Cutoff Errors in the Ewald Summation Formulae for Point Charge Systems. **1992**, *9*, 351–368.

(72) Frisch, M. J.; Trucks, G. W.; Schlegel, H. B.; Scuseria, G. E.; Robb, M. A.; Cheeseman, J. R.; Scalmani, G. et al. Gaussian[®]16 Revision C.01. 2016; Gaussian Inc. Wallingford CT.

(73) Eastman, P.; Behara, P. K.; Dotson, D. L.; Galvelis, R.; Herr, J. E.; Horton, J. T.; Mao, Y. et al. SPICE, A Dataset of Drug-like Molecules and Peptides for Training Machine Learning Potentials. *Sci. Data* **2023**, *10*, 11.

(74) Kingma, D. P.; Ba, J. Adam: A Method for Stochastic Optimization. **2017**,

(75) Pascanu, R.; Mikolov, T.; Bengio, Y. On the difficulty of training Recurrent Neural Networks. **2013**,

(76) Käser, S.; Boittier, E. D.; Upadhyay, M.; Meuwly, M. Transfer Learning to CCSD(T): Accurate Anharmonic Frequencies from Machine Learning Models. *J. Chem. Theory Comput.* **2021**, *17*, 3687–3699.

(77) Käser, S.; Richardson, J. O.; Meuwly, M. Transfer Learning for Affordable and High-Quality Tunneling Splittings from Instanton Calculations. *J. Chem. Theory Comput.* **2022**, *18*, 6840–6850.

(78) Hwang, W.; Austin, S. L.; Blondel, A.; Boittier, E. D.; Boresch, S.; Buck, M.; Buckner, J. et al. CHARMM at 45: Enhancements in Accessibility, Functionality, and Speed. *J. Phys. Chem. B* **2024**, *128*, 9976–10042.

(79) Boittier, E. D.; Devereux, M.; Meuwly, M. Molecular dynamics with conformationally dependent, distributed charges. *J. Chem. Theory Comput.* **2022**, *18*, 7544–7554.

(80) Boittier, E.; Töpfer, K.; Devereux, M.; Meuwly, M. Kernel-Based Minimal Distributed Charges: A Conformationally Dependent ESP-Model for Molecular Simulations. *J. Chem. Theory Comput.* **2024**, *20*, 8088–8099.

(81) Unke, O. T.; Meuwly, M. Toolkit for the Construction of Reproducing Kernel-based Representations of Data: Application to Multidimensional Potential Energy Surfaces. *J. Chem. Inf. Model.* **2017**, *57*, 1923–1931.

(82) Veliz, J. C. S. V.; Koner, D.; Schwilk, M.; Bemish, R. J.; Meuwly, M. The C(3P) + O₂($^3\Sigma_g$) \leftrightarrow CO₂ \leftrightarrow CO($^1\Sigma^+$) + O(1D)/O(3P) Reaction: Thermal and Vibrational Relaxation Rates from 15 K to 20000 K. *Phys. Chem. Chem. Phys.* **2021**, *23*, 11251–11263.

(83) Wang, B.; Truhlar, D. G. Partial Atomic Charges and Screened Charge Models of the Electrostatic Potential. *J. Chem. Theory Comput.* **2012**, *8*, 1989–1998.

(84) Hage, K. E.; Bereau, T.; Jakobsen, S.; Meuwly, M. Impact of Quadrupolar Electrostatics

on Atoms Adjacent to the Sigma-Hole in Condensed-Phase Simulations. *J. Chem. Theory Comput.* **2016**, *12*, 3008–3019.

(85) Vazquez-Salazar, L. I.; Boittier, E. D.; Unke, O. T.; Meuwly, M. Impact of the Characteristics of Quantum Chemical Databases on Machine Learning Prediction of Tautomerization Energies. *J. Chem. Theory Comput.* **2021**, *17*, 4769–4785.

(86) Itza Vazquez-Salazar, L.; D. Boittier, E.; Meuwly, M. Uncertainty quantification for predictions of atomistic neural networks. *Chem. Sci.* **2022**, *13*, 13068–13084.

(87) Yang, Z.; Huang, T.; Pan, L.; Wang, J.; Wang, L.; Ding, J.; Xiao, J. QuanDB: A Quantum Chemical Property Database towards Enhancing 3D Molecular Representation Learning. *J. Cheminf.* **2024**, *16*, 48.

(88) Tanimoto, T. T. *An Elementary Mathematical Theory of Classification and Prediction*; Technical Report, 1958; IBM Internal Technical Report.

(89) Stroet, M.; Caron, B.; Visscher, K. M.; Geerke, D. P.; Malde, A. K.; Mark, A. E. Automated Topology Builder Version 3.0: Prediction of Solvation Free Enthalpies in Water and Hexane. *J. Chem. Theory Comput.* **2018**, *14*, 5834–5845.

(90) Kong, L.; Park, S.-J.; Im, W. CHARMM-GUI PDB Reader and Manipulator: Covalent Ligand Modeling and Simulation. *J. Mol. Biol.* **2024**, *436*, 168554.

(91) Feng, S.; Park, S.; Choi, Y. K.; Im, W. CHARMM-GUI Membrane Builder: Past, Current, and Future Developments and Applications. *J. Chem. Theory Comput.* **2023**, *19*, 2161–2185.

5 Why Equivariance?

The advantage of equivariance is motivated with a simplified example, working in 3D space.³⁹ Consider a regression task aimed at predicting a set of scaled vectors pointing to the center of mass of three points (Fig. 7A). Here, a non equivariant three-layer feed-forward network with a hidden feature size of 21 and a two-layer equivariant network with a feature size of 3 are trained on points positioned in the xy -plane (Fig. 7). A validation set is constructed where the points can take arbitrary positions in 3D space. The standard neural network is unable to generalize to the validation set (Fig. 7B) because it did not see these rotated examples. In an ENN, the inputs in the training and validation sets are equivalent (albeit rotated) so the test and validation accuracy is comparable, and considerably lower than the standard NN in this toy example.^{41,42} Visualizing the hidden states of these networks provides some intuition to this different behavior (Figure 8). If the input X is permuted via a transpose to X^T (which corresponds to a valid rotation) the expected output Y should also be permuted to Y^T . However, the learned weight matrices of the NN cannot be permuted without causing the output to become incorrect (Figure 8A). In the equivariant example, if all $l = 1$ features of the input, hidden states, and output are visualized, the states of the neural network appear equivalent for X and X^T and only differ by transposition (Figure 8B). If data augmentation is applied by randomly rotating examples, the standard neural network is able to learn this simple function eventually; however, more data and longer training times are usually required to achieve results on par with ENNs.⁴⁹ Although this example is extremely contrived, it is common for quantum chemistry software to rotate a molecule to a ‘standard orientation’ (aligned to the principal axes of inertia) so such biases illustrated in the training/validation curves in Fig. 7A) may be introduced if data augmentation is not applied.³⁵

Considering the training loss (solid lines in Figures 7B and D), both NNs perform comparably although the ENN reaches considerably lower values. However, for the validation set (dashed lines), the non-ENN is unable to reach comparably low loss values whereas for the ENN the

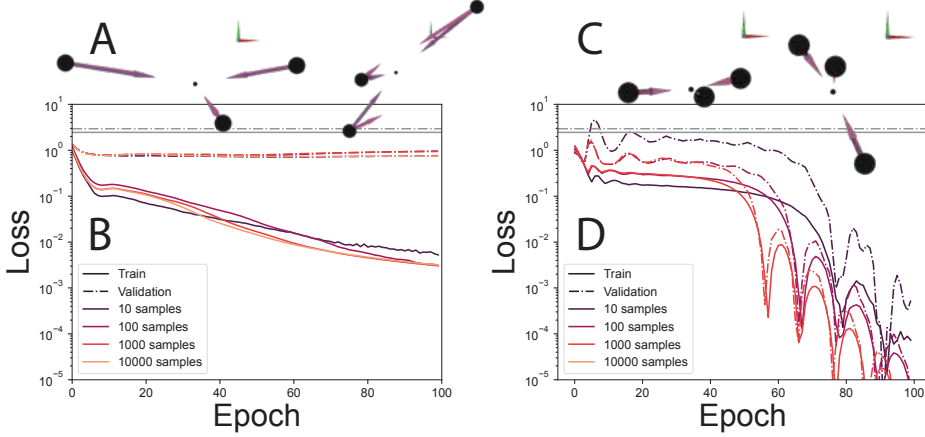


Figure 7: (A) Consider a simplified setting where the task is to predict atom-centered vectors pointing to the center of mass. (B) A feedforward neural network shown examples exclusively in the xy -plane is unable to generalize if a random rotation is applied to the validation set. (C) Prediction errors from equivariant neural networks (ENNs) are agnostic to global orientation. (D) As a result, ENNs can be more accurate and sample efficient when data is limited or training is costly.

loss on training and validation sets is comparable. If data augmentation is restrictive, for example due to training times, biases illustrated in the training/validation curves in Fig. 7A). In other words, using equivariant NNs may be a data reduction strategy.

6 Training Dynamics and Learning Curves

After initialization and even after the first training epoch, the predicted displacement vectors of the distributed charges have approximately zero magnitude, resulting in atom-centered charges. Atom centered charges are equivariant by definition and are a local minimum for the model. To elaborate, finding suitable displacements that generalize across the training set is difficult and atom centered solutions are a simple way to reduce the loss function early on during training. It was observed that, when using gradient clipping, constraining charge displacements and a small learning rate, it was possible to trap the models in this ‘atom-centered local minimum’ regime and subsequently converge the models to an accuracy on par with MBIS

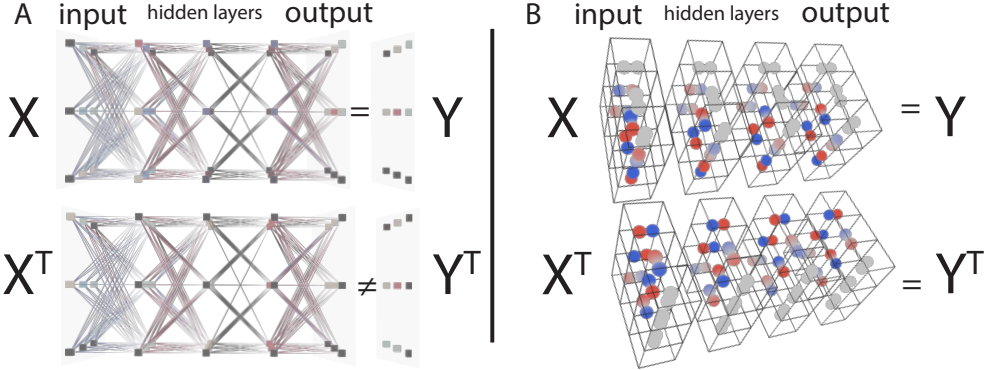


Figure 8: The input, hidden state, and output of a three-layer fully connected network with nodes and edges/weights colored by value for a NN (A) and (B) an ENN (only the $\ell_p = 1$ -features are depicted and the weights, i.e. coupling paths, are not shown for clarity). If the input X and output Y is transposed, the NN prediction is incorrect because the weights are insensitive to this transformation. For the ENN, since all operations are equivariant, the hidden states and output are equivalently transposed when shown X and X^T .

monopoles. However, by restarting training without gradient clipping or constraints on charge displacements, the models were able explore true distributed charge solutions and escape such local minima, after which the training could be restarted again with the original protocol.

An important approach in validating new approaches in deep learning is to verify the improvement of a model given more data, assuming there are no redundancies or conflicting information in the extended dataset.⁸⁶ According to statistical learning theory, a model should become more accurate when shown increasing amounts of data. This process exhibits a power-law relationship between the size of the data set and the accuracy of the model, which is also this case with DCM-net (Figure 10). The slope of the learning curves for models trained with w_{ESP} of 10^3 and 10^4 Hartree/ e are consistent when this prefactor is accounted for. This indicates that fitting to the ESP grid is a viable strategy for obtaining transferable distributed charge models. The variance in the learning curves is significant (Figure 10) due in part to the fact the models were trained on non-overlapping splits. The similar scaling performance observed for 3 and 4 charge models may be related to insufficient training, as the models were not fully converged after 500 epochs. The two charge models showed comparable

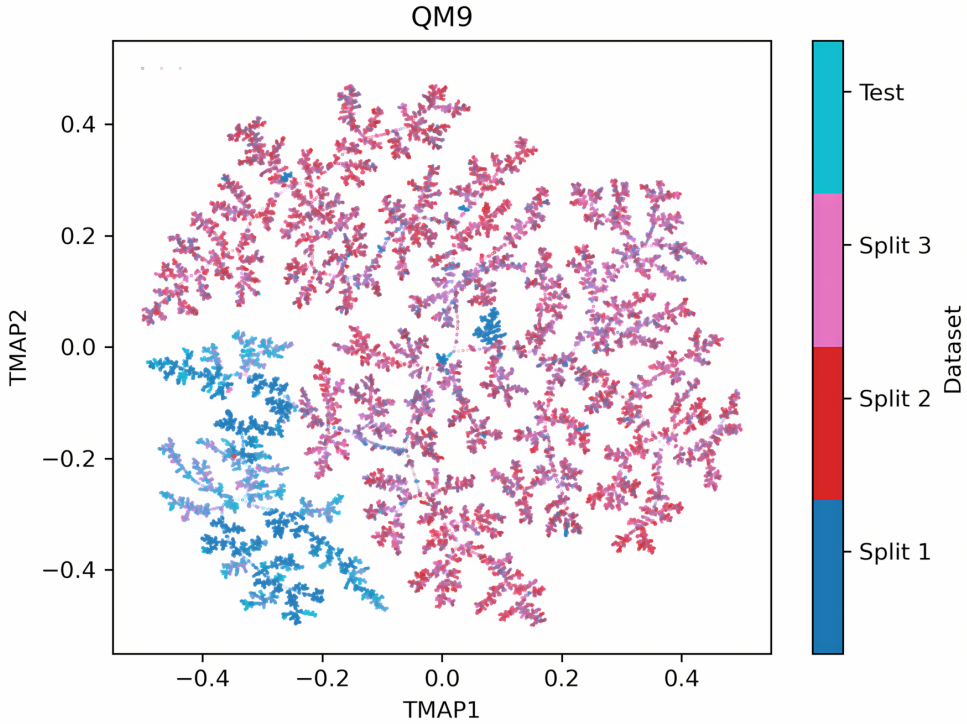


Figure 9: *Chemical space: QM9.*⁶² $TMAP^{65}$ projection of the dataset colored by split. Learning curves were generated from training on Splits 1 to 3 separately. Final models used all samples from Splits 1 - 3 in the training/validation splits. The test set contains atoms with either 8 or 9 heavy atoms. As observed in previous studies,⁸⁶ splitting by the order of the dataset introduces a sampling bias.

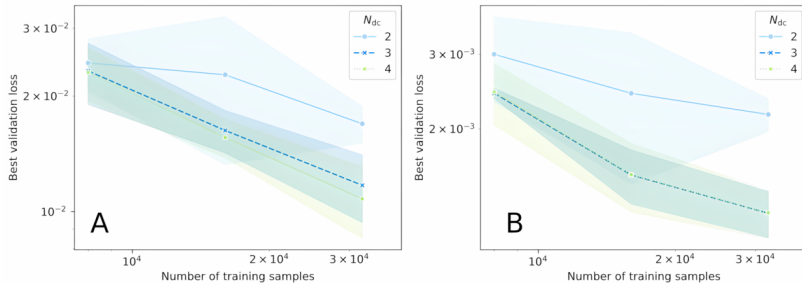


Figure 10: Learning curves for shorter training runs (500 epochs) with an ESP weight w of 10^4 (A) and 10^3 (B) using three non-overlapping splits of the data. Shaded areas report the standard deviation for three splits of the training data. Different colors/line styles are for different values of n_{DC} : between 2-4 distributed charges per atom.

validation loss with that of the three and four charge models in the low data regime (< 20k training samples) which demonstrates the variance in the performance of the models. This

observation reinforces the point that finding a set of distributed charges that reproduces the ESP is non-unique.

7 QM9: Training Data Distributions and Chemistry

Following on from the main text, more details on the training data distributions and chemistry are provided. Figure 11 shows the distribution of point charges for the test set using MBIS (black), CGenFF (gold), and DCM-net (green). The distribution of charges for the DCM-net model is similar to that of MBIS, indicating that the model is able to learn the correct charges for the test set.

Table 5 shows the average RMSE_{ESP} $((\text{kcal/mol})/e)$ evaluated on grid points grouped by proximity to the nearest CGenFF atom type using fitted MBIS multipole expansions. Errors less than 0.5 $(\text{kcal/mol})/e$ are shown in bold. The average RMSE_{ESP} for the DCM-net model is similar to that of MBIS, indicating that the model is able to learn the correct charges for the test set.

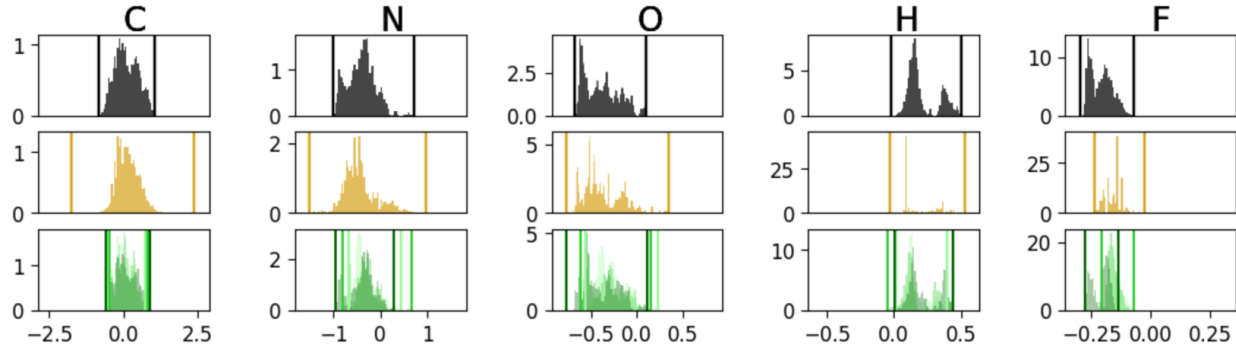


Figure 11: Distribution of point charge magnitudes (e) for the test set using MBIS (black), CGenFF (gold), and DCM-net (green). Vertical bars show the range of the charge values.

Table 5: The average RMSE_{ESP} ((kcal/mol)/*e*) evaluated on grid points grouped by proximity to the nearest CGenFF atom type using fitted MBIS multipole expansions. Errors less than 0.5 (kcal/mol)/*e* are shown in bold.

	<i>l</i> = 0	<i>l</i> \leq 1	<i>l</i> \leq 2	description
CG1N1	1.34	0.71	0.48	Carbon in cyano group
CG1T1	1.42	0.61	0.42	Alkyne carbon (R-C)
CG1T2	0.84	0.38	0.25	Alkyne carbon (H-C)
CG2R71	2.59	0.64	0.42	7-membered aromatic carbon
FGA3	0.20	0.06	0.04	Aliphatic fluorine, trifluoro group
FGR1	0.50	0.16	0.10	Aromatic fluorine
HGA1	0.50	0.12	0.08	Aliphatic proton, CH
HGA2	0.40	0.11	0.07	Aliphatic proton, CH2
HGA3	0.31	0.09	0.06	Aliphatic proton, CH3
HGP1	0.49	0.12	0.08	Polar hydrogen
HGP4	0.43	0.09	0.06	Polar hydrogen, neutral conjugated -NH2 group
HGPAM1	0.49	0.17	0.11	Polar hydrogen, neutral dimethylamine group
HGPAM2	0.37	0.08	0.05	Polar hydrogen, neutral methylamine group
HGR51	0.47	0.12	0.08	Nonpolar hydrogen, neutral 5-membered planar ring carbon
HGR52	0.47	0.13	0.09	Aldehyde hydrogen, formamide hydrogen (RCOH)
HGR61	0.45	0.16	0.11	Aromatic hydrogen
HGR62	0.50	0.16	0.11	Nonpolar hydrogen, neutral 6-membered planar ring
NG1T1	0.31	0.18	0.12	Nitrogen in cyano group
NG2D1	1.09	0.29	0.20	Nitrogen in neutral imine
NG2R50	0.66	0.16	0.11	Double-bonded nitrogen in neutral 5-membered planar ring
NG2R60	0.79	0.27	0.18	Double-bonded nitrogen in neutral 6-membered planar ring
NG2R62	0.77	0.22	0.15	Double-bonded nitrogen in 6-membered planar ring with heteroatoms
NG321	1.76	0.37	0.26	Neutral methylamine nitrogen
OG2D1	0.56	0.16	0.11	Carbonyl oxygen
OG2D4	0.72	0.17	0.12	6-membered aromatic carbonyl oxygen
OG2R50	0.76	0.19	0.13	Oxygen in furan ring
OG301	1.49	0.37	0.25	Ether oxygen (-O-)
OG311	0.84	0.18	0.12	Hydroxyl oxygen
OG3R60	1.01	0.31	0.21	Oxygen in 6-membered cyclic enol, ether, or ester

Table 6: The average RMSE_{ESP} ((kcal/mol)/*e*) evaluated on grid points grouped by proximity to the nearest CGenFF atom type using trained DCM-net models with the best performance on the training set. Errors less than 0.5 (kcal/mol)/*e* are shown in bold.

	<i>n_{dc}</i> = 2	3	4	description
CG1N1	1.30	1.13	1.16	Carbon in cyano group
CG1T1	1.45	1.12	1.16	Alkyne carbon (R-C)
CG1T2	0.80	0.70	0.63	Alkyne carbon (H-C)
CG2R71	2.32	2.41	2.00	7-membered aromatic carbon (e.g., azulene)
FGA3	0.19	0.17	0.15	Aliphatic fluorine, trifluoro group
FGR1	0.40	0.29	0.31	Aromatic fluorine
HGA1	0.34	0.28	0.29	Aliphatic proton, CH
HGA2	0.27	0.21	0.24	Aliphatic proton, CH ₂
HGA3	0.23	0.20	0.21	Aliphatic proton, CH ₃
HGP1	0.36	0.31	0.33	Polar hydrogen
HGP4	0.31	0.22	0.22	Polar hydrogen, neutral conjugated -NH ₂ group
HGPAM1	0.44	0.38	0.37	Polar hydrogen, neutral dimethylamine group
HGPAM2	0.27	0.25	0.24	Polar hydrogen, neutral methylamine group
HGR51	0.38	0.34	0.39	Nonpolar hydrogen, neutral 5-membered planar ring carbon
HGR52	0.36	0.32	0.34	Aldehyde hydrogen, formamide hydrogen (RCOH);
HGR61	0.41	0.32	0.34	Aromatic hydrogen
HGR62	0.40	0.31	0.33	Nonpolar hydrogen, neutral 6-membered planar ring
NG1T1	0.32	0.27	0.29	Nitrogen in cyano group
NG2D1	0.88	0.76	0.78	Nitrogen in neutral imine
NG2R50	0.48	0.42	0.46	Double-bonded nitrogen in neutral 5-membered planar ring
NG2R60	0.57	0.47	0.49	Double-bonded nitrogen in neutral 6-membered planar ring
NG2R62	0.61	0.48	0.49	Double-bonded nitrogen in 6-membered planar ring with heteroatoms
NG321	1.28	1.21	1.18	Neutral methylamine nitrogen
OG2D1	0.45	0.37	0.39	Carbonyl oxygen
OG2D4	0.47	0.37	0.37	6-membered aromatic carbonyl oxygen
OG2R50	0.58	0.50	0.57	Oxygen in furan ring
OG301	0.99	0.80	0.79	Ether oxygen
OG311	0.56	0.45	0.48	Hydroxyl oxygen
OG3R60	0.76	0.62	0.63	Oxygen in 6-membered cyclic enol, ether, or ester

TOC Graphic

